Article:
Yue, X, Liu, H, Zhao, Y et al. (7 more authors) (2021) The evolution and characterisation of the corrosion scales formed on 3Cr steel in CO2-containing conditions relevant to geothermal energy production. Corrosion Science, 183. 109342. ISSN 0010-938X

https://doi.org/10.1016/j.corsci.2021.109342

The evolution and characterisation of the corrosion scales formed on 3Cr steel in CO_2-containing conditions relevant to geothermal energy production

Yong Hua[a]*, Xiaoqi Yue[c], Huifeng Liu[a, b], Yang Zhao[d], ZeZhou Wen[a], Yongxing Wang[a], Tao Zhang[d]*, Lei Zhang[c]*, Jianbo Sun[b]* and Anne Neville[a]

a: Institute of Functional Surfaces, School of Mechanical Engineering, University of Leeds, Leeds, LS2 9JT, United Kingdom.
b: School of Materials Science and Engineering, China University of Petroleum (East China), Qingdao, China.
c: Institute of Advanced Materials and Technology, University of Science and Technology Beijing, Beijing, 100083, China.
d: Shenyang National Laboratory for Materials Science, Northeastern University, 3-11 Wenhua Road, Shenyang 110819, China.

*Corresponding author: Yong Hua: Y.Hua@leeds.ac.uk;
Tao Zhang: zhangtao@mail.neu.edu.cn;
JianboSun: sunjianbo@upc.edu.cn.
Zhang Lei: zhanglei@ustb.edu.cn;

Abstract

The corrosion behaviour of 3Cr steel at CO_2 partial pressures (p_{CO2}) of 2.7/28.5 bar and 200°C was investigated. The evolution of double-layered corrosion scales was analysed by surface analysis to identify physical and chemical nature and results are combined with an analysis of thermodynamic calculations. Both experimental and thermodynamic results show that the corrosion scales comprise a crystalline $FeCO_3$ outer layer and an inner Fe_3O_4, $FeCr_2O_4$, and $Cr(OH)_3$ at 2.7 bar p_{CO2}. At 28.5 bar p_{CO2}, the inner layer evolves to be a mixture of $FeCr_2O_4$ and $Cr(OH)_3$ containing concentrated Cl^- ions, and this induces an enhancement of localised corrosion.

Keywords: 3Cr steel, CO_2 corrosion, corrosion scales, inner layer evolution

1.0 Introduction

The corrosion behaviour of pipeline and tubing steels in CO_2-containing geothermal environments has received significant attention, yet the control of material corrosion remains an important issue for researchers due to the essentially complicated corrosion processes.[1] Considering economic savings, to find a low-cost material with improved corrosion resistance is one of the logical and key strategies for corrosion control to geothermal energy production.

Several researchers reported the variation of chromium (Cr) content on influence of corrosion resistance for different low alloy tubing. [1-10] To date, researchers have considered to replace carbon steel by 1-5% Cr steels based on their improved corrosion resistance and enlarge the scope of applications. This is important as demands for corrosion resistance material from renewable energy sources such as geothermal. Materials must provide the required performance while proving to be an economic alternative. Recently, 3Cr steel has become one of the common potential candidates because it is significantly cheaper than stainless steel and has promising improved corrosion protection compared to carbon steel within oil and gas application.

Several works have been conducted to evaluate the corrosion behaviour in terms of general and localised corrosion of 3Cr steels under high temperature and high pressure (HTHP) environments and to understand the corrosion mechanisms or the corrosion product formation in CO_2-saturated aqueous environments.

1.1 Research reviews relevant to general corrosion behaviour of 3Cr steels in CO_2 environments

Xu et al.[1] investigated the corrosion behaviour of two 3Cr steels (Bainite-Ferrite (BF) and Ferrite-Pearlite (FP) microstructures) in CO_2-saturated conditions at 80 °C and 8 bar. They found that the

formation of the corrosion product scales reduces corrosion rates and suggested that the observed low corrosion rates are attributed to enrichment of Cr within the corrosion scales which this layer can protect to the steel. Their report recommended that BF-3Cr steels provide better corrosion resistance than FP-3Cr steels. Muraki et al.[2] indicated that an increase in Cr level from 0 to 5% progressively decreases the general corrosion rates, and mainly due to forming protective corrosion product scales and suggested that this enriched Cr layer effectively suppresses the general corrosion rate. Takabe and Ueda[3] compared the general corrosion rates of low Cr-bearing steels in the CO_2 environment a 60 °C and 100 °C with test periods of 24, 48, 96 and 720 hours. Results showed that the general corrosion rate was reduced by increasing the Cr content and the enriched Cr was observed in the protective corrosion product scales. Kermani et al.[4] reported the corrosion behaviour of 3Cr steel for 1 and 22 months in actual field conditions and the results indicated that the protective Cr rich layer on the steel surface is stable and capable of forming at a relatively low pH such as 3.8. One important message from Kermani et al's[4] work for 3% Cr steel was related to the economics of the alloy, 3Cr steel has less than 1.5 times cost penalty compared to conventional grades of carbon steel, with promising improved corrosion protection by 3 to 40 times compared to carbon steel in oil & gas applications. Zhu et al.[5] tracked the film growth at 80 °C and 8 bar of p_{CO2} via the EIS method and divided the formation processes of the film into three periods; dynamic adsorption, an incomplete-coverage film and a fully covered film. Their results suggested that the fast dissolution process of 3Cr steels mainly occurs in the first 2 hours with the absence of film or the surface was covered by an incomplete-coverage film. Guo et al's work[6] in the same condition further clarified that corrosion product scales include an inner $Cr(OH)_3$ layer (containing nano-quasicrystalline and nanocrystalline grains) and outer $FeCO_3$ crystals precipitated on the inner layer,

suggesting that the decrease in anodic dissolution current over long periods was due to the inner layer than the outer $FeCO_3$ layer. Lu et al.,[7] used electrochemical measurements to examine 3Cr steels under 3 bar CO_2 at various temperatures up to 90 °C. Their corrosion rates increased with rising the temperatures. A double-structure corrosion product layer was observed at low temperatures of 30-50 °C, it can be noted that a single $FeCO_3$ layer was reported at 70-90 °C.

Liu et al.[8] conducted long-term corrosion tests from 168 hours to 1008 hours at 80°C, 2.3 bar CO_2 partial pressure, and a velocity of 2.5 m/s and the results suggested that a three-layered structure can be observed. Both inner and outer layers are identified as $FeCO_3$, and the enrichment of Cr is exhibited in a cement-like middle layer and mixture with $FeCO_3$. Li et al.,[9] performed corrosion tests on 3Cr exposed to CO_2-saturated solutions at 8 bar CO_2 and 80 °C for 240 hours. They reported that 3Cr with a martensite microstructure has the best corrosion resistance compared to other types of 3Cr with bainite or ferrite/pearlite microstructure. Wang et al.,[10] indicated that the addition of Ca^{2+} can change the morphology and composition of the corrosion products on the surface. The initial corrosion rates were measured smaller due to the presence of Ca^{2+} compared to that of the absence of Ca^{2+} condition, suggesting the Ca^{2+} ions accelerate the precipitation of initial corrosion scales. As for the harsh conditions for low Cr bearing alloys, Hua et al.[11] reported the poor corrosion resistance of low Cr steels, including 3Cr, at 60°C and 100 bar CO_2 and indicated that the low Cr steels cannot provide better corrosion resistance compared to X65 carbon steel over long term exposure.

1.2 *Research review on the localised corrosion behavior of 3Cr steels in CO_2 environments*

In 2001, Takabe and Ueda[3] studied the corrosion product formation for C-Mn steel and 1-5% Cr steels with martensitic microstructure at 60 °C and 100 °C and various immersion times. The results indicated that the Cr content within the inner corrosion product scale increases from 12.5% to 50 % mass Cr. 3Cr and 5Cr steels provide better localised corrosion resistance than 1Cr steel. The work of Chen et al.[12] showed that Cr content in the steel increased up to 4% results in improved pitting resistance. The formation of protective corrosion scales is comprised of $Cr(OH)_3$, Cr_7C_3, $FeCO_3$ and Cr_2O_3 and the inner layer is mainly $Cr(OH)_3$. The results suggested that the inner layer was responsible for significantly improving the pitting resistance. Lin et al.,[13] conducted experiments for 3Cr exposed to the solution containing CO_2-O_2. They reported that the presence of O_2 reduces the corrosion product protection to the steel surface. The dissolved 5% O_2 increases the pitting corrosion occurring on the surface due to the measured nonuniform Cr-rich areas. Wei et al.,[14] performed the experiments for X70, 3Cr and 6.5Cr steels exposed to CO_2-saturated solution at 80 °C and pressure of 100 bar. The results indicated that the additional 3Cr increases the general corrosion rate, but the localised corrosion decreases under the flow rate of 1 m/s. The corrosion rates were decreased significantly as Cr content increased to 6.5 wt.%. An inner Cr-rich layer was proved to protect the localised corrosion. The results from Hua et al.[11] in a 100 bar CO_2 condition suggested that the Cr-riched inner layer formed on 3Cr and 5Cr steels appears to accelerate the pit propagation. The formation of the inner layer with increasing Cr content is less dense and compact compared with $FeCO_3$ formed on carbon steel thus failed to improve localised corrosion resistance at 60°C and CO_2 partial of 100 bar. Similarly, the results of Liu et al.[8] revealed the $Cr(OH)_3$ locally co-precipitated with $FeCO_3$ over long exposure times and the presence of co-precipitated corrosion scales increases the localised corrosion.

Based on the literature above, 3Cr steel is considered as an improved corrosion resistance alternative to carbon steel, whilst it is significantly cheaper than stainless steels. However, little information exists in the literature relating to the corrosion behaviour in terms of general and localised corrosion for 3Cr steels exposed to conditions that reflect geothermal environments (where temperatures > 150 °C). The purpose of this research is to fill this knowledge gap via studying the protective capability of the corrosion product scales formed on 3Cr steel surfaces at various CO_2 partial pressures as well as the corrosion capabilities of 3Cr steel in terms of the general and localised corrosion behaviour under a high temperature (200°C) CO_2 environment. We have also merged the results from the detailed characterisation of the physical and chemical nature of the corrosion scales with an analysis of Pourbaix diagrams. We propose a CO_2 corrosion mechanism for 3Cr steels immersed in CO_2-saturated solution, clarifying that the Cl^- ions induce localised corrosion at HTHP.

2.0 Experimental procedure

2.1 material and methods

The elemental compositions of 3Cr steel are 0.21 wt.% Si, 0.24 wt.% C, 0.005 wt.% P, 0.0015 wt.% S, 0.53 wt.% Mn, 3.1 wt.% Cr and balance with Fe, its microstructure as shown in Figure 1. The disc sample with a 25 mm diameter and 5 mm in thickness.

The sample surface was wet-ground to 1200 grit SiC abrasive paper. It was then abraded with a 3µm diamond suspension to achieve a mirror finish. According to the ASTM E3-01[15] and E407-99 standards[16], the etchant solution was 3% Nital and the sample was immersed in the Nital solution

for 15s. The microstructure image of 3Cr steel was performed via a LEICA DM 6000M upright optical microscope. Carbides are randomly distributed within the 3Cr steel as shown in Figure 1.

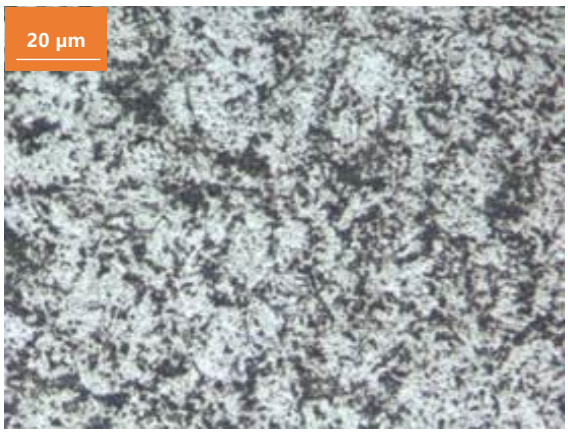

Figure 1. The microstructure of 3Cr steel.

Figure 2 represents the whole autoclave setup. The experimental procedure can be found in our previous publications[17, 18]. The ratio of the volume of the solution to the sample area was 33mL/cm^2. The experimental matrix is provided in Table 1. The predicted pH and Pourbaix diagrams were calculated by using OLI software.[24] The considered species to generate the diagrams have been provided in Table S1 in the supplementary document.

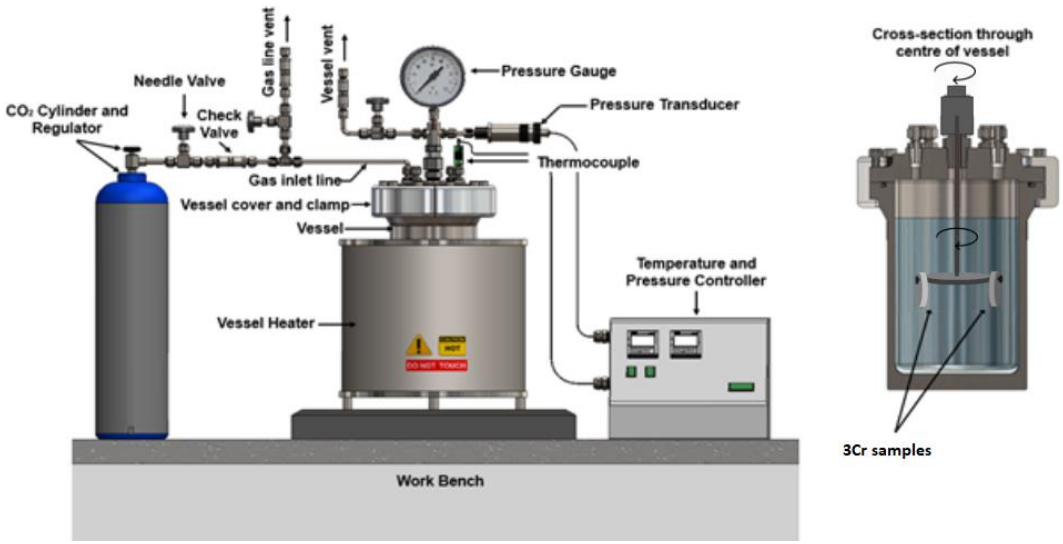

Figure 2. A schematic diagram of the experimental setup for the corrosion tests. [17, 18]

145 **Table 1: Test conditions**

Brine (mg/L)	Temp, °C	CO_2 pressure at 25 °C, bar	pH	CO_2 pressure at 200°C, bar	Total pressure at 200°C, bar	Immersion time, hours
NaCl solution: Cl-: 29503, NaHCO3:585	200	1	6.41	2.7	18	5/20/48/120
		20	5.39	28.5	46	

146

147 After immersion tests, the autoclave was cooled down to 80 °C within 10 minutes, followed by the
148 depressurisation of the vessel. The corroded specimens were immediately rinsed with distilled
149 water and dried with compressed air. The corrosion scales were removed according to ASTM G1-03
150 standards[19] using Clark's solution (20 g antimony trioxide + 50 g tin(II) chloride + 1000 ml 38%
151 hydrochloric acid). The corrosion rate was calculated by the following equation.

$$R_{\mathrm{corr}} = \frac{8.76 \times 10^7 \times \Delta m}{S \times T \times \rho} \quad (1)$$

152 Where R_{corr} is the general corrosion rate, mm/year; Δm is the weight loss, g; S is the exposed surface
153 area, cm^2; ρ is the density of the steel, g/cm^3; and T is the immersion time, hours.

154 ***2.2 Surface analysis***

155 One sample with covered corrosion scales from each condition was used to perform surface analysis.
156 The characterisation of morphology and chemical composition via a combination of scanning
157 electron microscopy (SEM), energy-dispersive X-ray spectroscopy (EDX) throughout a Carl Zeiss EVO
158 MA15 SEM combined with a focused ion beam (FIB) would contribute an important part of this study.
159 In addition, the composition and state of naturally formed corrosion scales were analysed by X-ray
160 diffraction (XRD) and Raman spectroscopy respectively.

After the removal of corrosion scales, profilometry measurements were conducted by an NPFLEX 3D Surface Metrology System. According to ASTM Standard G46-94 [20], the top 10 deepest pits were used for the pitting depth characterisation of scanned areas from each sample. The localised corrosion rates were calculated by using Equ (2)

$$Rr_{\mathrm{L}} = \frac{8.76 \times D}{T} \quad (2)$$

Where Rr_L is the localised corrosion rate, mm/year; D is the average localised/pitting depth of ten deepest pits from the sample in μm; T is immersion time in hours.

3.0 Results

3.1 Effect of p_{CO2}

The total mass loss values and average corrosion rates of 3Cr steels at 2.7 and 28.5 bar of p_{CO2} at 200°C after 5, 20, 48, and 120 hours of exposure are provided in Figure 3. The results indicate that 3Cr steel has the highest corrosion rates of 2.86 and 7.67 mm/year in the first 5 hours for 2.7 and 28.5 bar CO_2 partial pressure, respectively. The high corrosion rates in the first 5 hours suggest the fast dissolution of the metal ions from the 3Cr matrix. The average corrosion rates gradually decline over time, reaching 0.26 and 0.33 mm/ year after 120 hours for 2.7 bar and 28.5 bar of p_{CO2} respectively.

The slowly increased mass losses between 5 hours and 20 hours result in a sharp drop of the initial corrosion rates, suggesting the corrosion product scales formed on the surface and protected the 3Cr surface from the corrosion. The mass loss for 3Cr gradually was recorded from 12.83 to 27.88 g/m^2 between 5 hours and 120 hours at 2.7 bar of p_{CO2}, but it is stable at around 35.67 g/m^2 under 28.5 bar of p_{CO2} over this period, suggesting the different protectiveness of the corrosion scales

formed on the surface at various p_{CO2}.

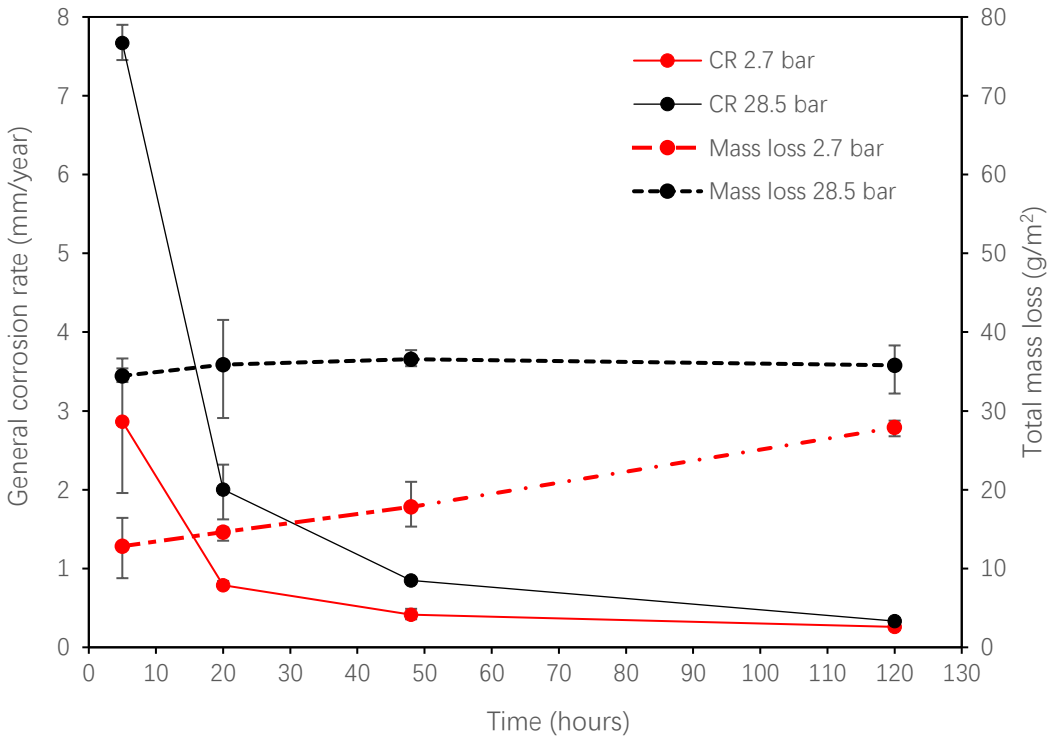

Figure 3. The total mass loss values and average corrosion rates for 3Cr steels at 2.7 and 28.5 bar of p_{CO2} at 200°C after 5, 20, 48, and 120 hours of exposure

3.2 Characterisation of corrosion scales developed on the surface at both p_{CO2}

Figure 4 represents the morphology of the corrosion product scales formed on the surface after 5, 20, 48 and 120 hours. The crystals are found after 5 hours of exposure at both conditions. The crystals at 2.7 bar of p_{CO2} are randomly distributed (Figure 4a) in comparison to the situation at p_{CO2} of 28.5 bar where the 3Cr surface is completely covered by corrosion scales. The scatter crystals on the surface significantly increased in number from 20 to 48 hours at 2.7 bar of CO_2 (Figure 4 c and e), followed by increasing in size after 120 hours as shown in Figure 4g.

Under the high p_{CO2} of 28.5 bar, in-complete surface coverage was observed after 5 hours of exposure, gaps between the corrosion scales were found. 3Cr surface is covered by dense and

compact corrosion scales after 20 hours of exposure, and there are no visible differences for the corrosion product scales after generating the compact and dense scales on the surface after 20 hours as shown in Figures 4f and 4h.

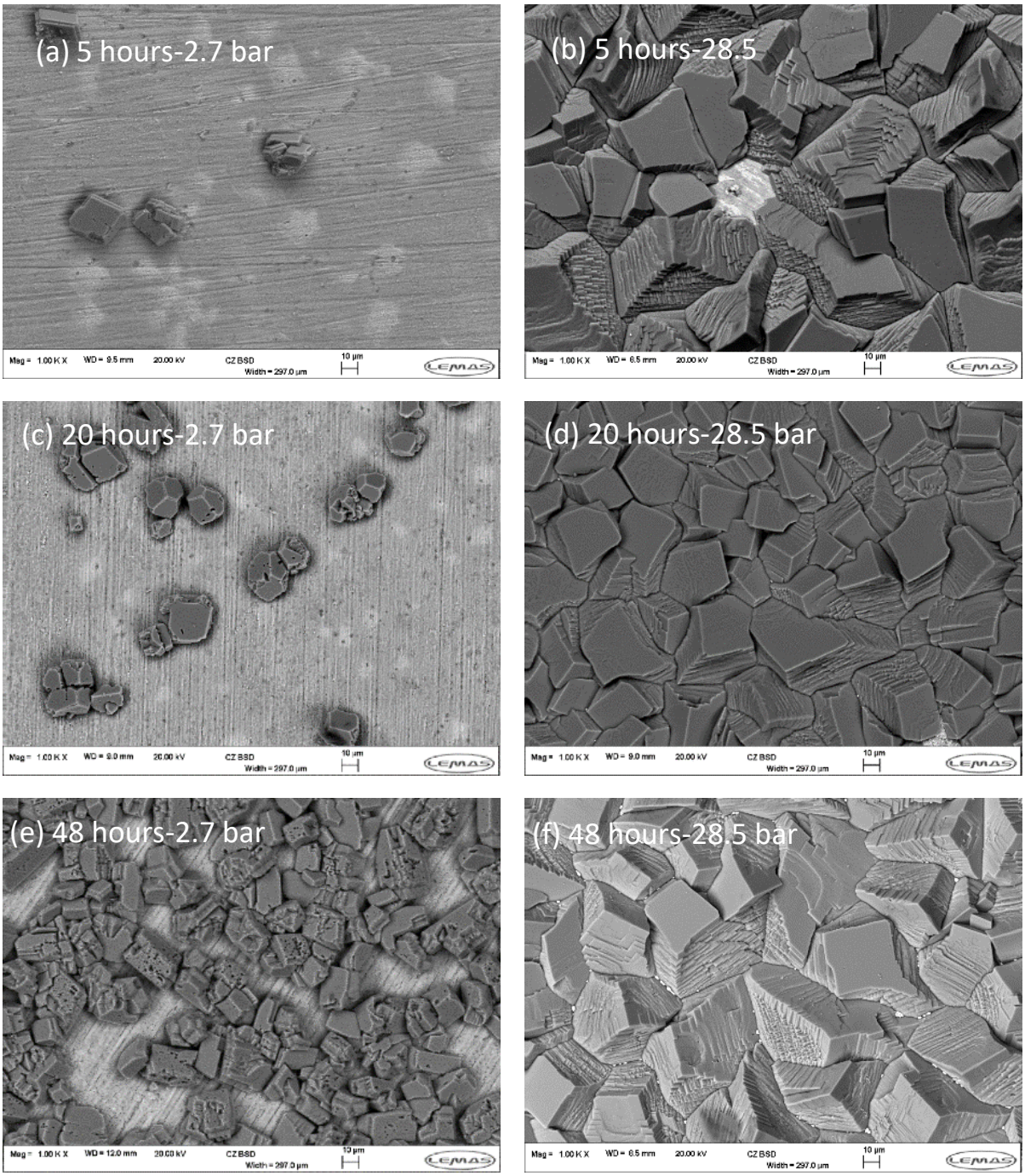

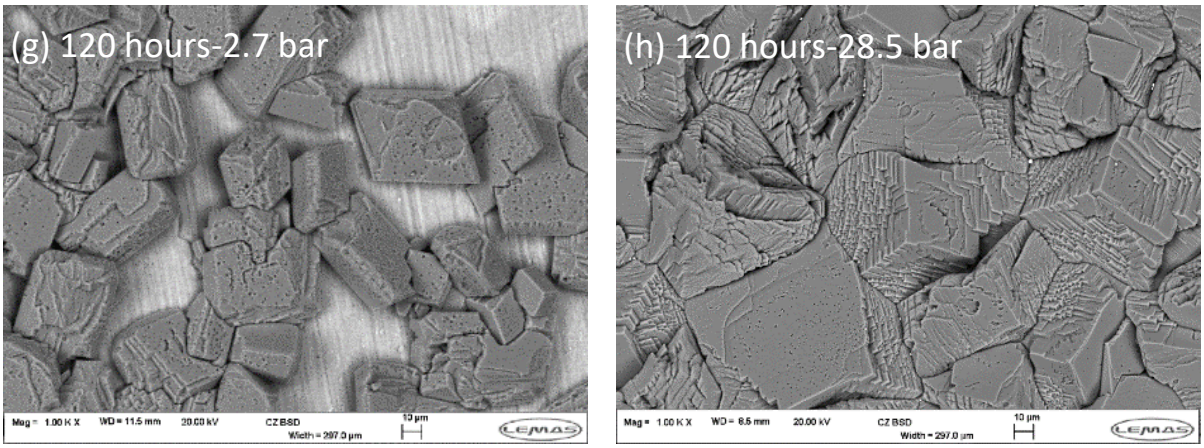

Figure 4. Surface morphology of 3Cr steels at 200°C under different p_{CO2} with different immersion time.

In Figure 5, the cross-section SEM images of corrosion product scales formed at p_{CO2} of 2.7 bar and 28.5 bar and different immersion times are presented. For 2.7 bar $p_{CO2,}$ the outer crystals are found after 5 hours of exposure while the inner layer is thin and approximately around 1µm. After 20 hours, the thickness of the inner layer increased locally to 2-3 µm. The inner corrosion layer is non-uniformly developed over the immersion time.

For 28.5 bar $p_{CO2,}$ the inner corrosion film is distributed non-uniformly with a thickness range between 0.1 and 5 µm over the various immersion times.

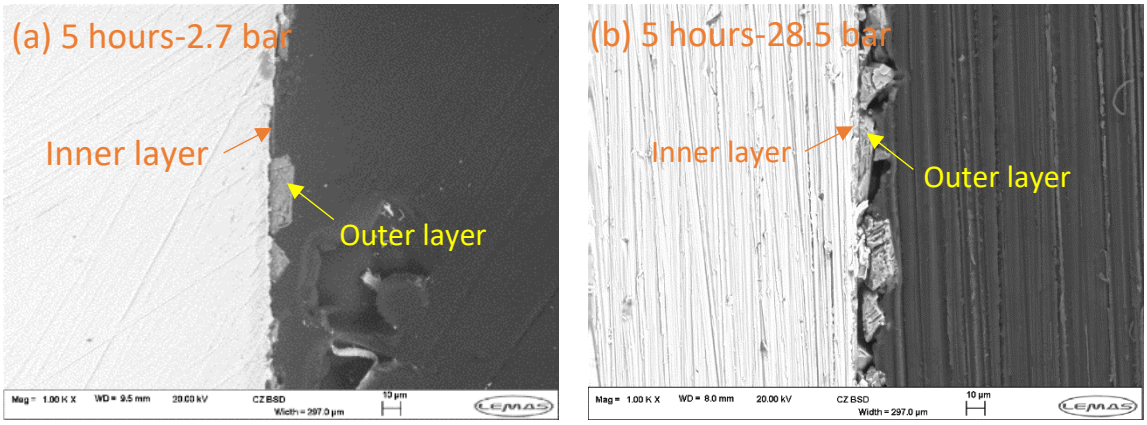

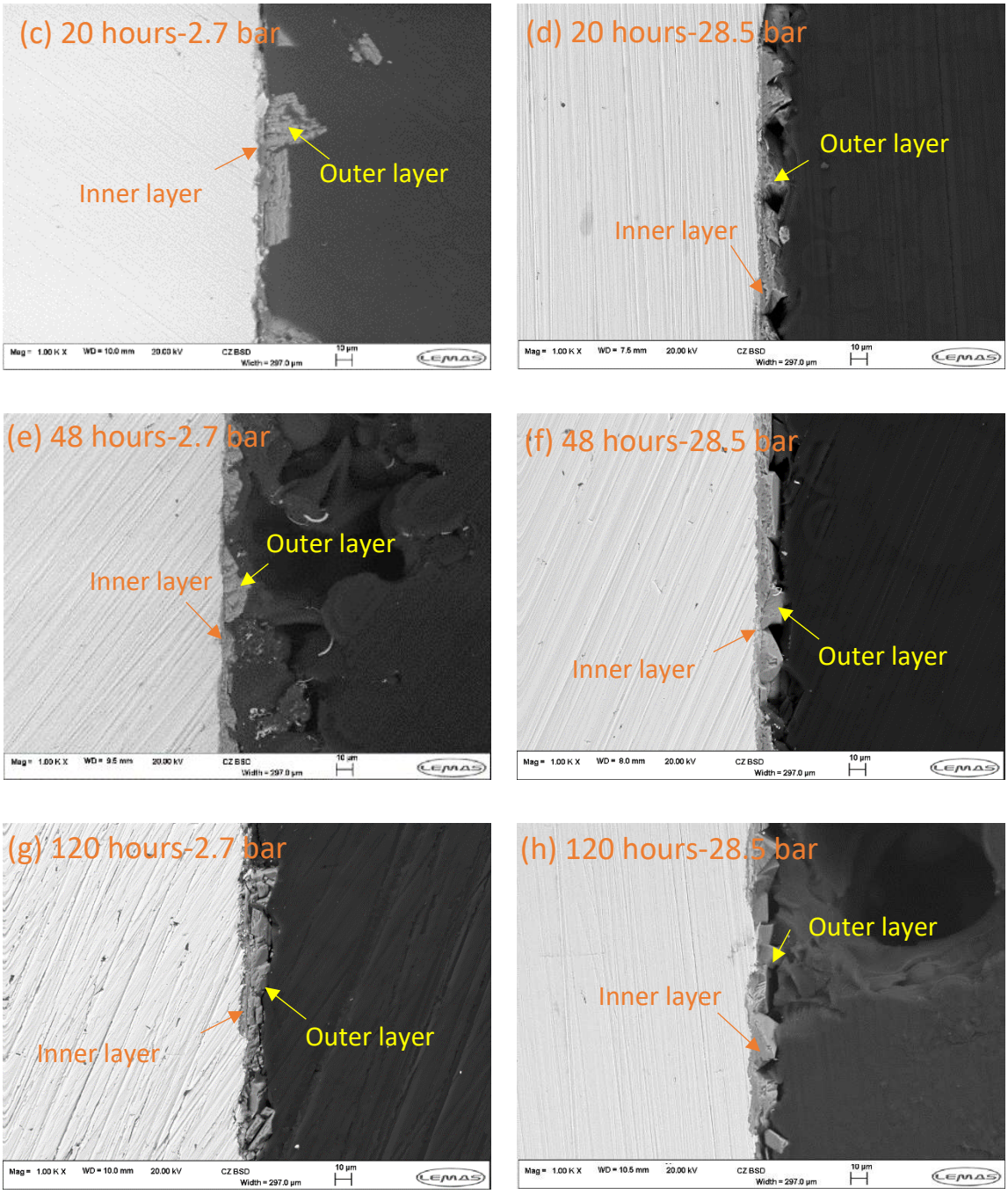

Figure 5. Cross-section images of 3Cr steel at 200°C under different p_{CO2} with different immersion time.

Figure 6 illustrates the elemental distribution for the double-layered scales formed on 3Cr steel after 20 hours and 120 hours of exposure at 200°C and 2.7 bar of CO_2. The outer crystalline layer is comprised of Fe, O and C compounds and precipitated on a Cr-enriched inner layer. It can be seen

that the high chromium content accumulated at the matrix/inner layer interface after 20 hours and 120 hours.

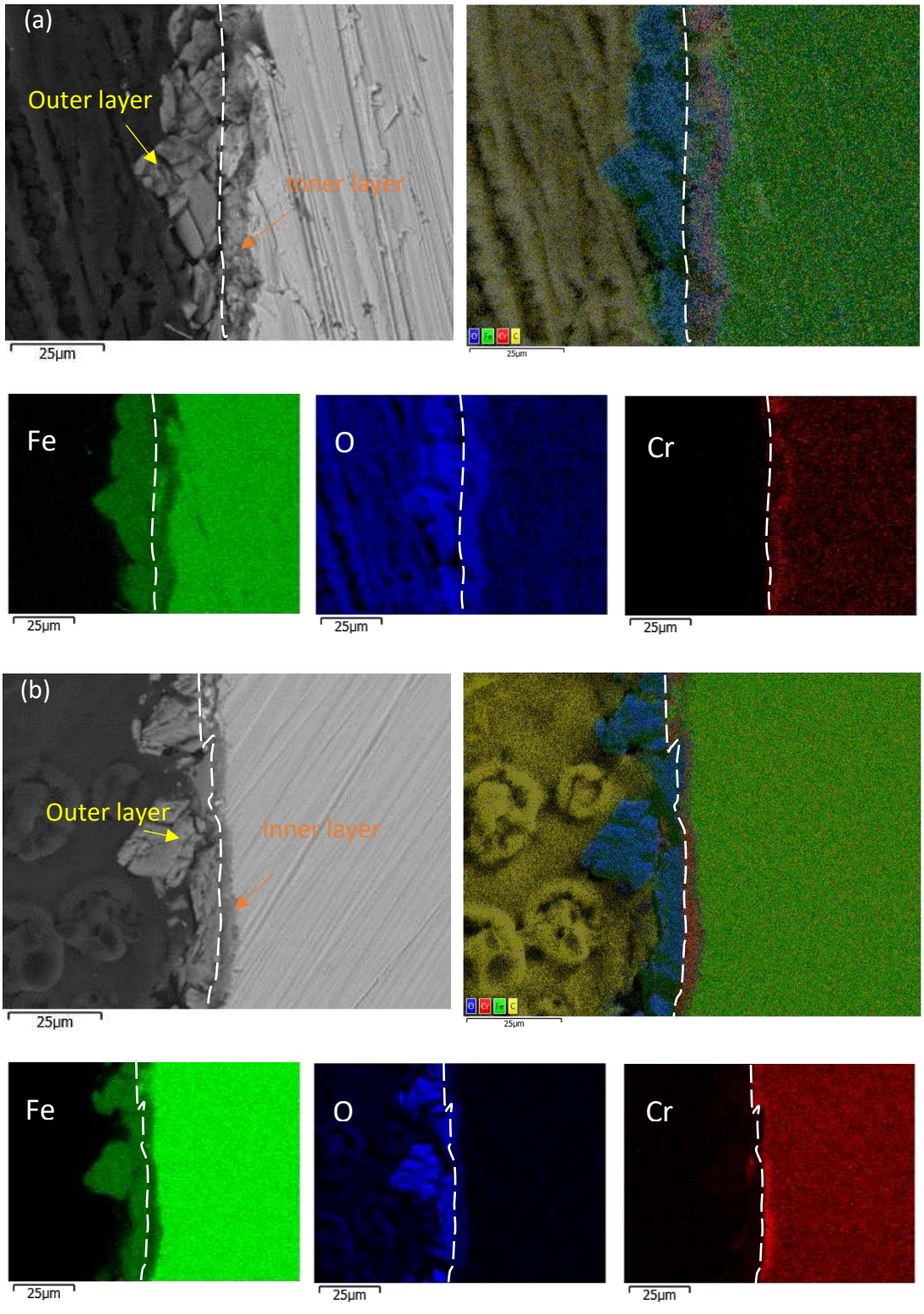

Figure 6. Elemental distribution of double-layered scale formed on 3Cr steel in (a) 20 hours and (b) 120 hours at 200°C and 2.7 bar p_{CO2}.

A similar Cr-rich inner layer was detected on the 3Cr steel surface at 200°C and 28.5 bar of p_{CO2} as shown in Figure 7. A high concentration of Cr layer was observed throughout the inner layer after 20 hours. The development of the outer layer becomes uniform and the overall thickness of the corrosion product layers is 20-25 µm over 120 hours of exposure.

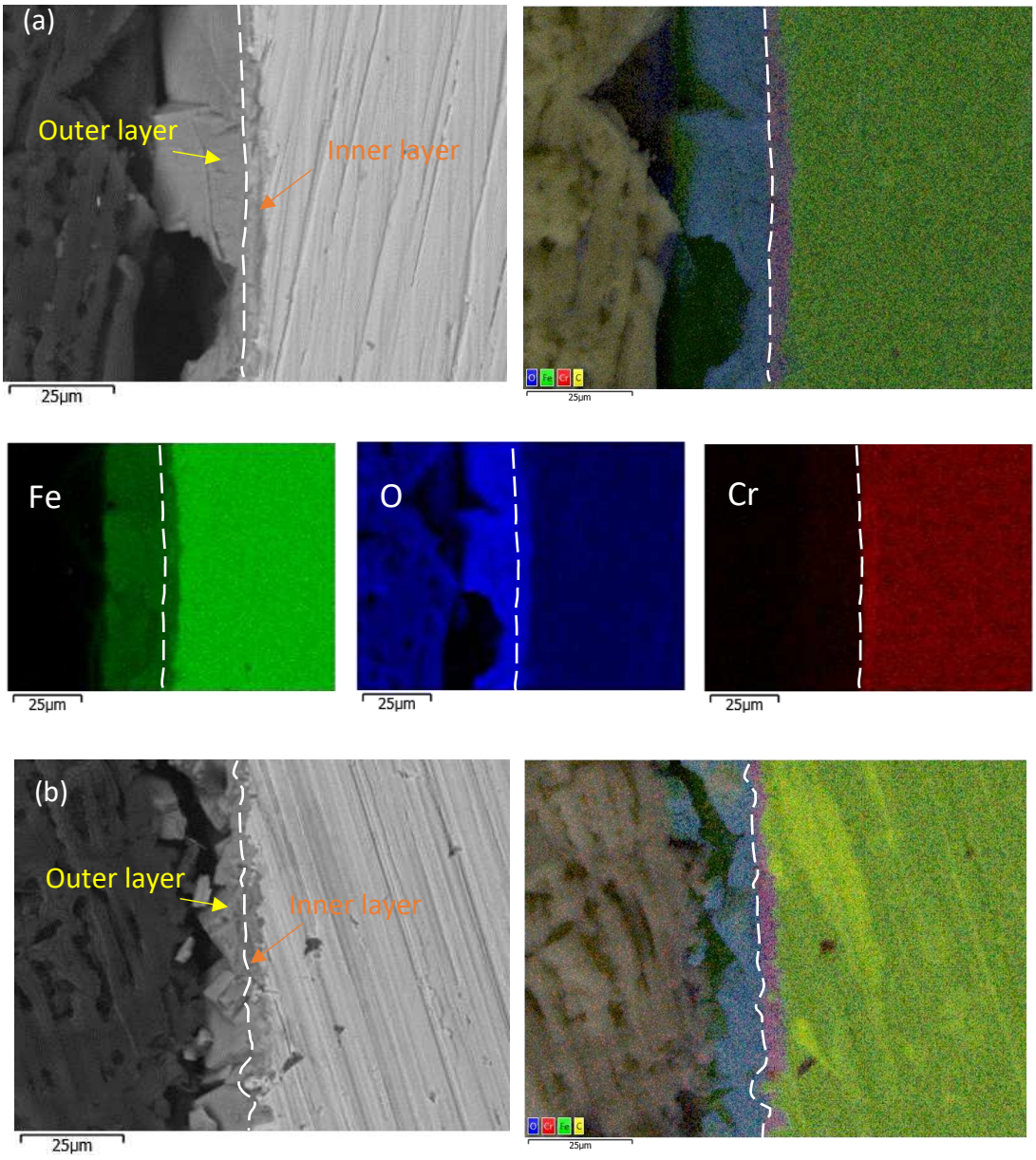

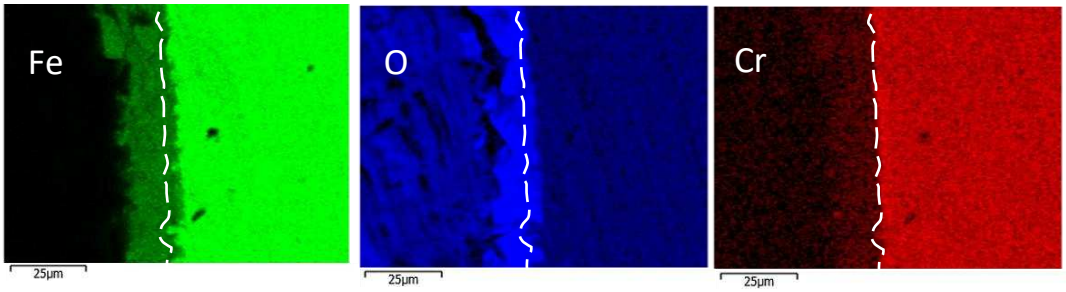

Figure 7. Elemental distribution of double-layered scales formed on 3Cr steel in (a) 20 hours and (b) 120 hours at 200°C and 28.5 bar p_{CO2}.

A combination of Raman spectroscopy and XRD was employed to determine the composition of the corrosion scales developed on the steel surface at various immersion times. Fig. 8 shows the XRD patterns of the corrosion scales formed on the surface for both p_{CO2}, highlighting that the detected dominant crystalline phase on the steel surface is $FeCO_3$. In Figure 8a, it is interesting to note that the intensity of the Fe peak located at 44.5° decreased with the enhanced $FeCO_3$ peaks (are located at 24.8° and 32.1°) as the exposure time is prolonged. The results suggest that the thickness of the crystalline $FeCO_3$ increased via the precipitation processes at p_{CO2} of 2.7 bar. Moreover, a peak located at around 35.5° is detected which belongs to a spinel structure at various immersion times. Previous studies reported that the peak at 35.5° is typical spinel (Fe_3O_4 or $FeCr_2O_4$)[21]. However, the indistinguishable diffraction peaks for these corrosion scales require further tests to determine the composition.

As the p_{CO2} increased to 28.5 bar, only $FeCO_3$ and Fe peaks were detected on the surface as shown in Figure 8b and the peak intensities show no differences at various immersion times.

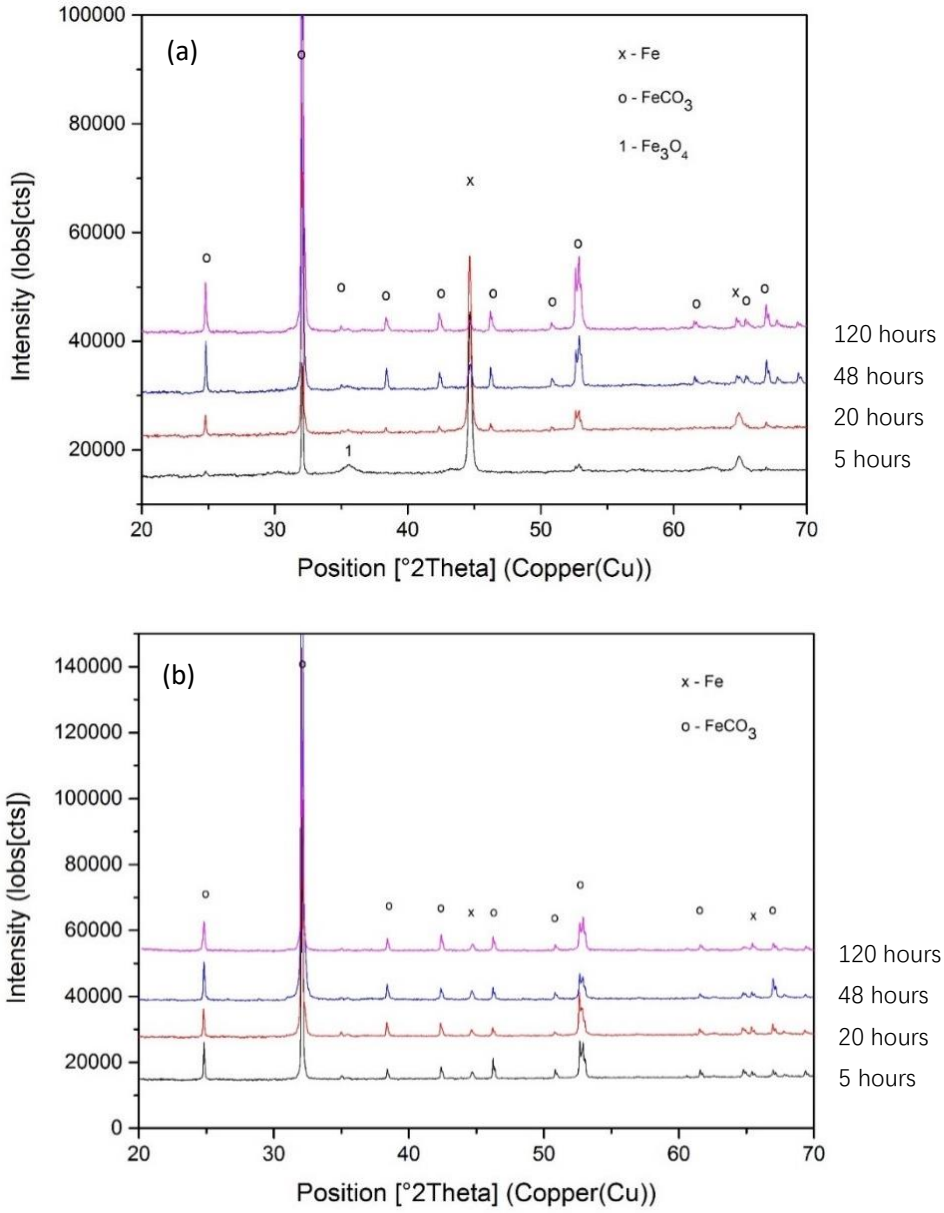

Figure 8. XRD of 3Cr steel with different immersion times at 200°C, (a) 2.7 bar and (b) 28.5 bar p_{CO_2}.

The Raman spectra for samples exposed to the CO_2-saturated solution at various immersion times are provided in Figure 9. For 2.7 bar p_{CO_2}, the results in Figure 9a indicate that the precipitation of the outer $FeCO_3$ crystals is located at 1086 cm^{-1} and the inner Fe_3O_4 layer is at 667 cm^{-1} from 5 to 48 hours of exposure. It is interesting to note that the peak is located at 667 cm^{-1} becoming wider after 48 hours and implies the formation of the mixed compounds for the inner layer over longer

immersion times. The local Raman spectra was measured via the cross-section as shown in Figure 9a confirmed that the inner layer contains $FeCr_2O_4$ and $Cr(OH)_3$ after 120 hours, which in agreement with EDS measurements that a rich-Cr inner layer is detected as shown in Figure 6.

For the corrosion product scales formed on the surface at 28.5 bar of CO_2 (Figure 9b), similar to the results for 2.7 bar of p_{CO2}, the double-layered scales are comprised of a $FeCO_3$ outer layer and the inner layer insisting of both $Cr(OH)_3$ and $FeCr_2O_4$.

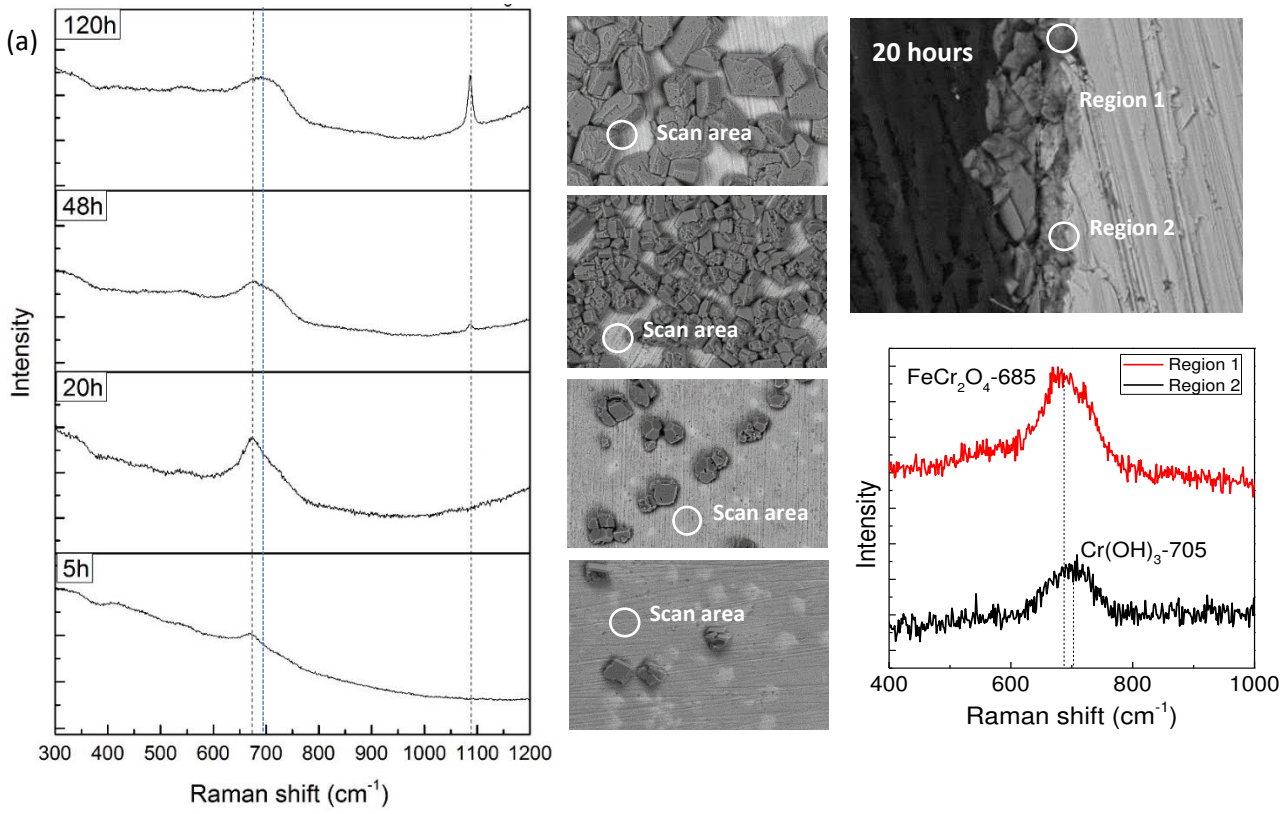

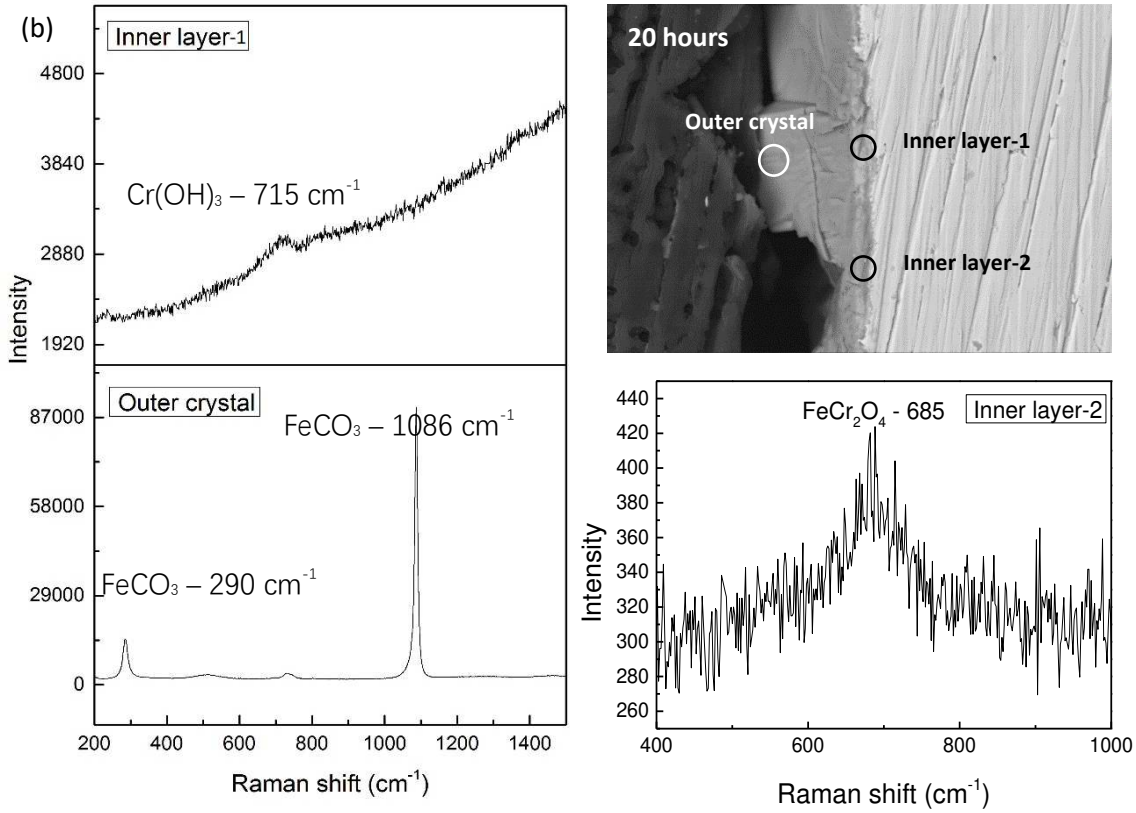

Figure 9. Raman spectra of 3Cr steel with different immersion time at 200°C and (a) 2.7 bar CO_2, (b) 28.5 bar CO_2.

3.3 Localised corrosion behaviour of 3Cr steels immersed to the CO_2-saturated solution at p_{CO2} of 2.7 and 28.5 bar

After the removal of the corrosion scales from the surface according to ASTM G 01-03[19], profilometry was performed on the surface and the average pitting depths were calculated by considering the top 10 deepest pits from each sample. The results are provided in Figure 10. For p_{CO2} of 2.7 bar, the average pit depth increased from 2.5 to 5.3 µm between 5 and 120 hours; this suggests that the pits grow slowly at low p_{CO2}. Conversely, an average pitting depth of 11.6 µm was measured after 5 hours at the condition of 28.5 bar p_{CO2}, and it increased slightly to 13.4 µm after 20 hours. The pit depth maintains relatively stable at approximately 13.7 µm after 120 hours with the formation of the double-layered corrosion product scales on the surface.

The examples of 2D profilometry images of 3 mm x 3 mm scanned areas from the 3Cr surface are provided in Figure 10. The results exhibit that 3Cr suffers a higher localised corrosion attack at 200°C and 28.5 bar p_{CO2} compared to low p_{CO2} of 2.7 bar. There is no obvious development of the localised corrosion attack over the immersion time at 2.7 bar. However, the increased p_{CO2} from 2.7 bar to 28.5 bar, resulting in the level of localised attack is 5 times higher and suggests that the localised corrosion rates become severe with increasing p_{CO2}.

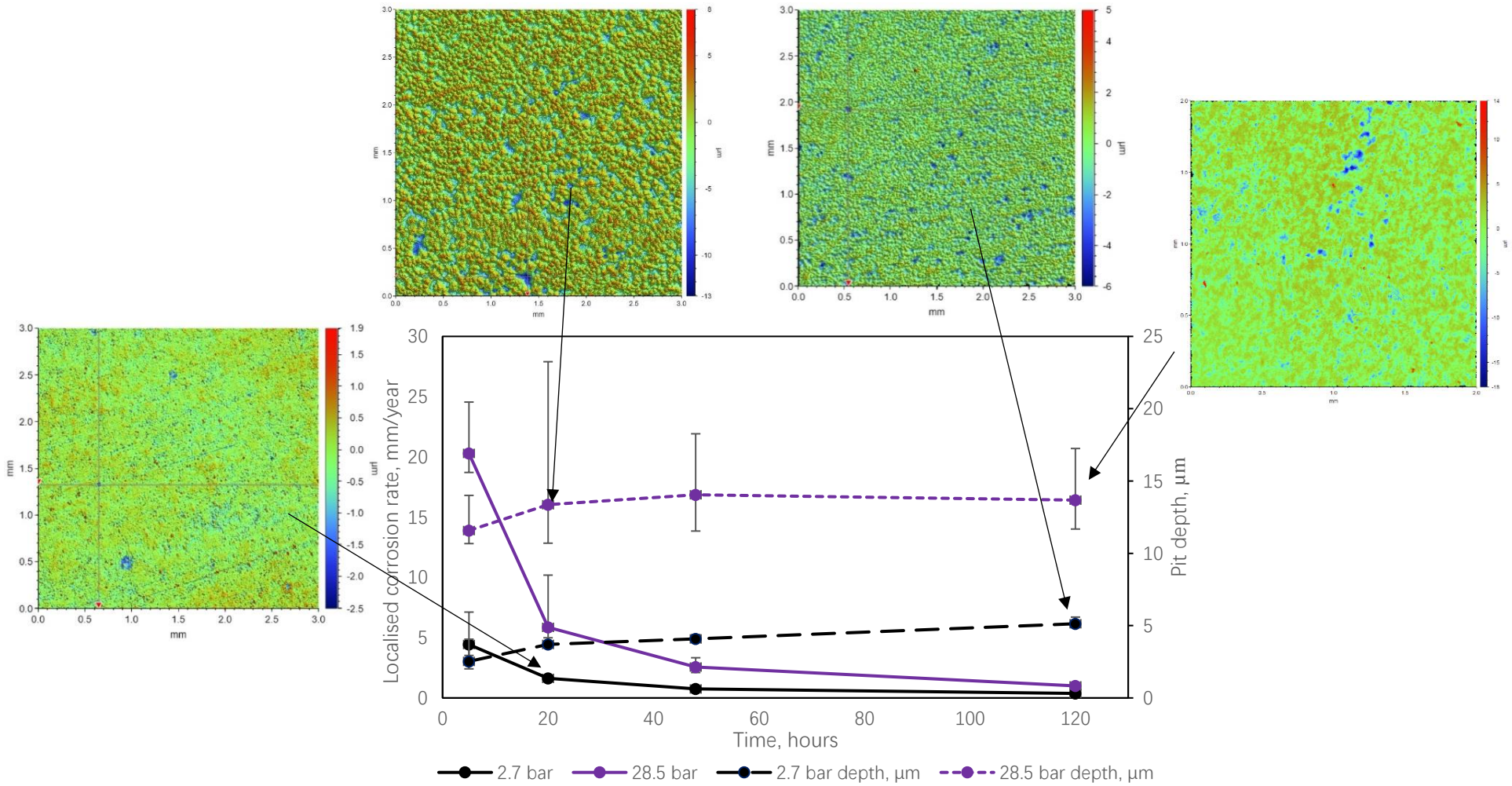

Figure 10. Profilometry of 3Cr steel after 5, 20, 48 and 120 hours of exposure at 200°C and p_{CO2} of 2.7 and 28.5 bar respectively.

Figure 11 shows the surface morphology of the sample after the removal of the corrosion scales. As shown in Figure 11 a and c, localised/pitting was observed on the surface after 5 and 20 hours of exposure at p_{CO2} of 2.7 bar. The pits on the surface develop onto large and wide localised corrosion over-long immersion periods as shown in Figure 11 g. For the 28.5 bar of p_{CO2}, the pits are randomly distributed on the surface in the early stages. It can be seen that the sample surface suffers localised attack over long-term exposure.

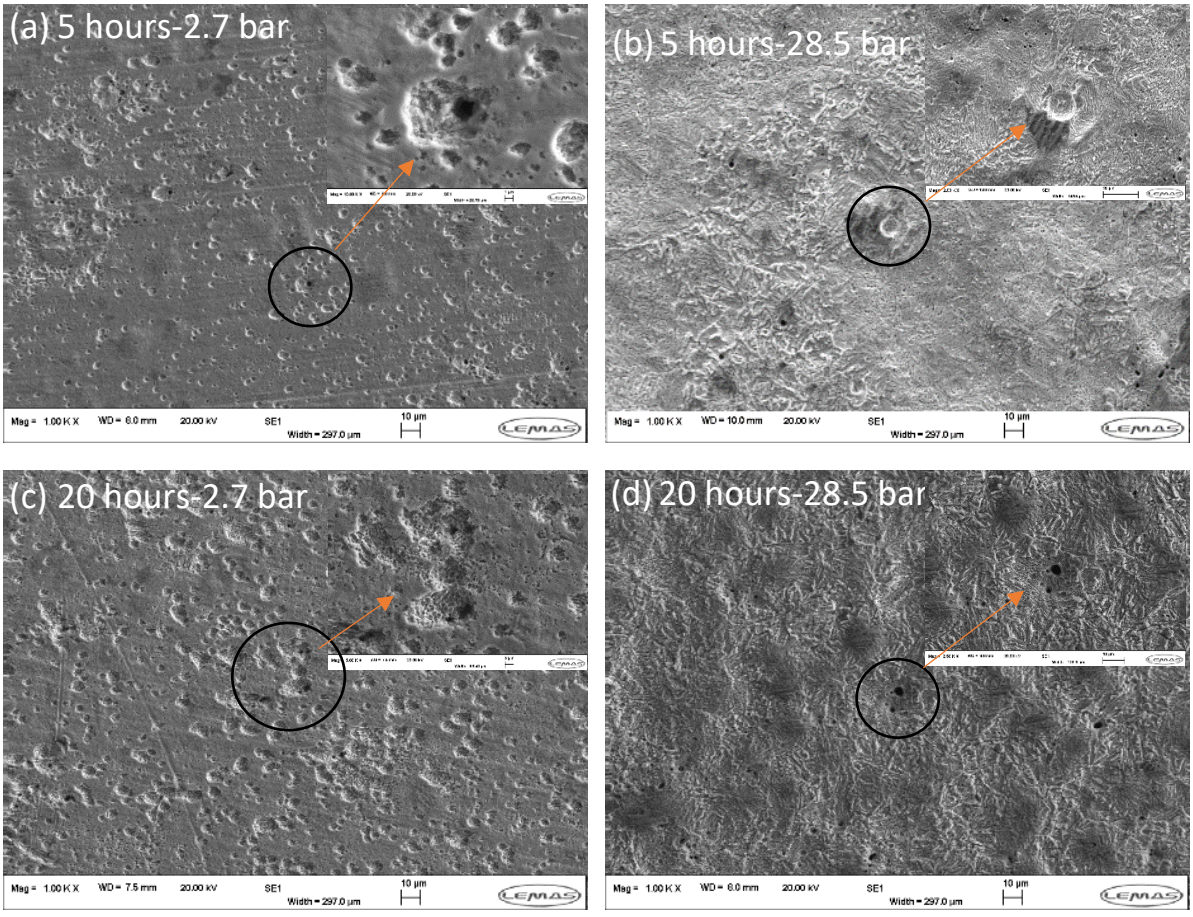

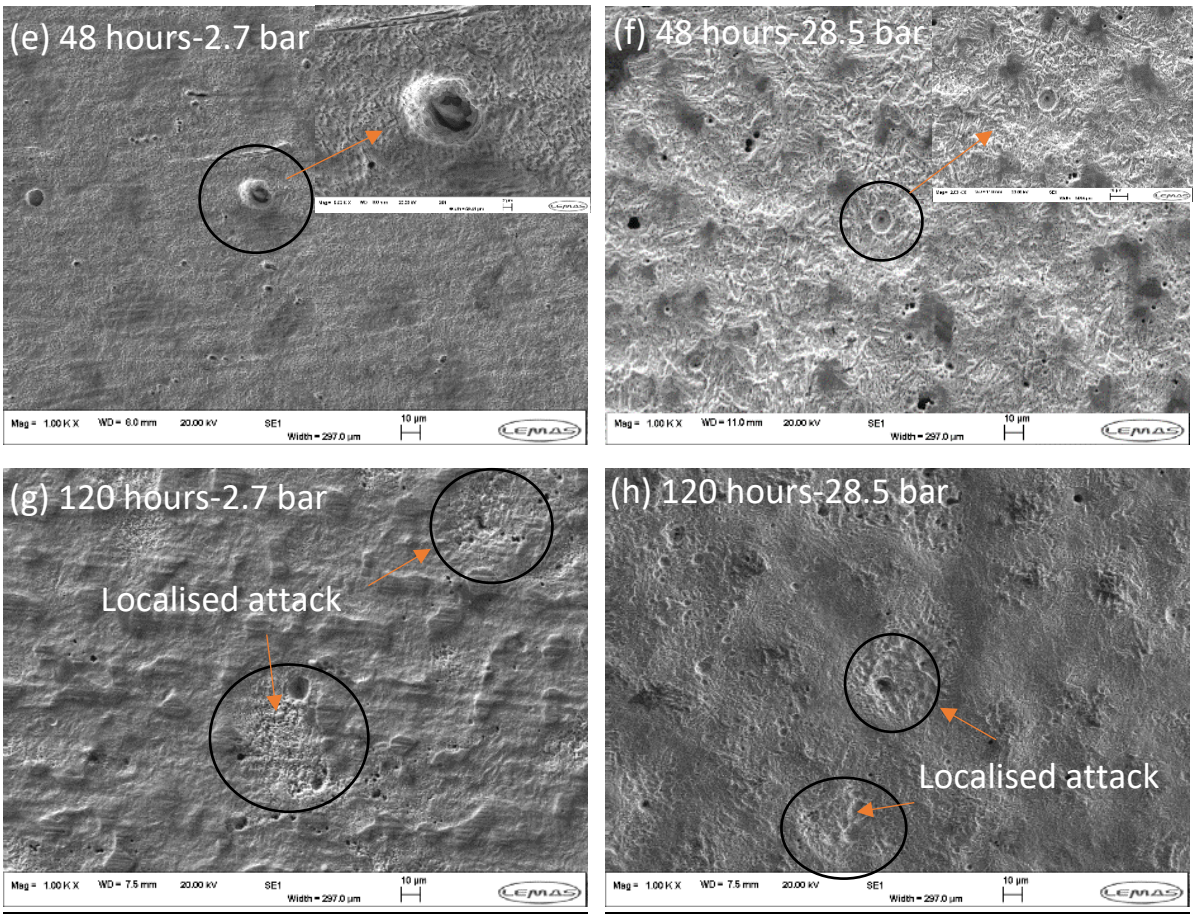

288 **Figure 11. SEM images of 3Cr steel after removing corrosion scales after 5, 20, 48 and 120**

289 **hours of exposure at 200°C and p_{CO2} of 2.7 and 28.5 bar.**

290 ***3.4 Characterisation of the localised corrosion and inner corrosion layer at steel interface***

291 To further understand the correlation between the measured localised corrosion and the

292 corrosion product scales formed on the 3Cr surface, FIB combined with high-resolution SEM

293 and EDS were applied. The cross-section prepared by FIB provides the analysis region of the

294 corrosion scales formed on the surface at 200°C and 2.7 bar of p_{CO2} as shown in Figure 12.

295 Figure 12b exhibits the inner layer is approximately 1 µm in thickness, and it covered the

296 entire surface including the areas beneath the outer crystalline $FeCO_3$, suggesting good

297 general corrosion protection to the steel surface (Figure 3). However, the localized/pits were

observed at the matrix/inner layer interface in regions 1 and 2 (Figure 12b). The line-scans in regions 1 and 2 show no obvious Cl^- ion distributed in the inner layer, indicating a relatively mild localised corrosion for 3Cr steel at 200°C and 2.7 bar of p_{CO2} without the acceleration by Cl^-, consistent with the observation of the localised corrosion shown in Figure 11.

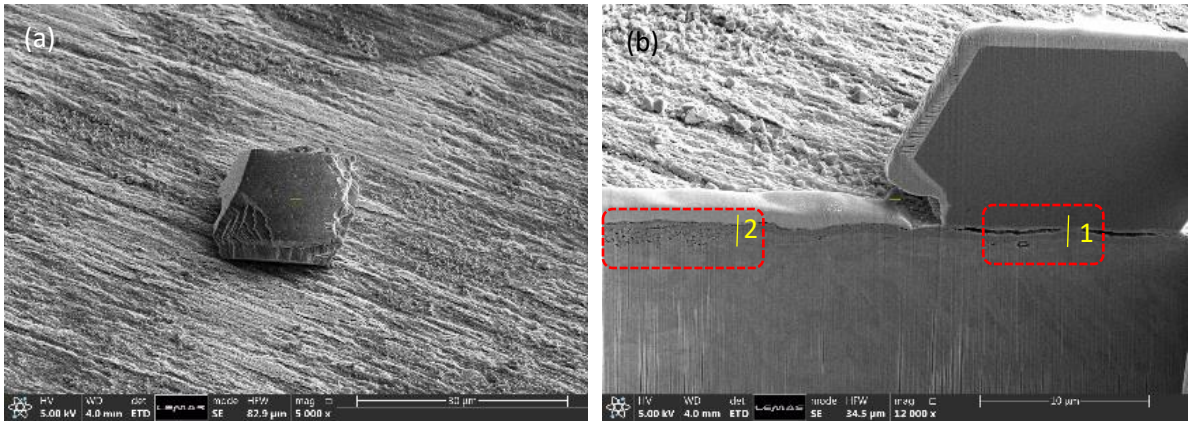

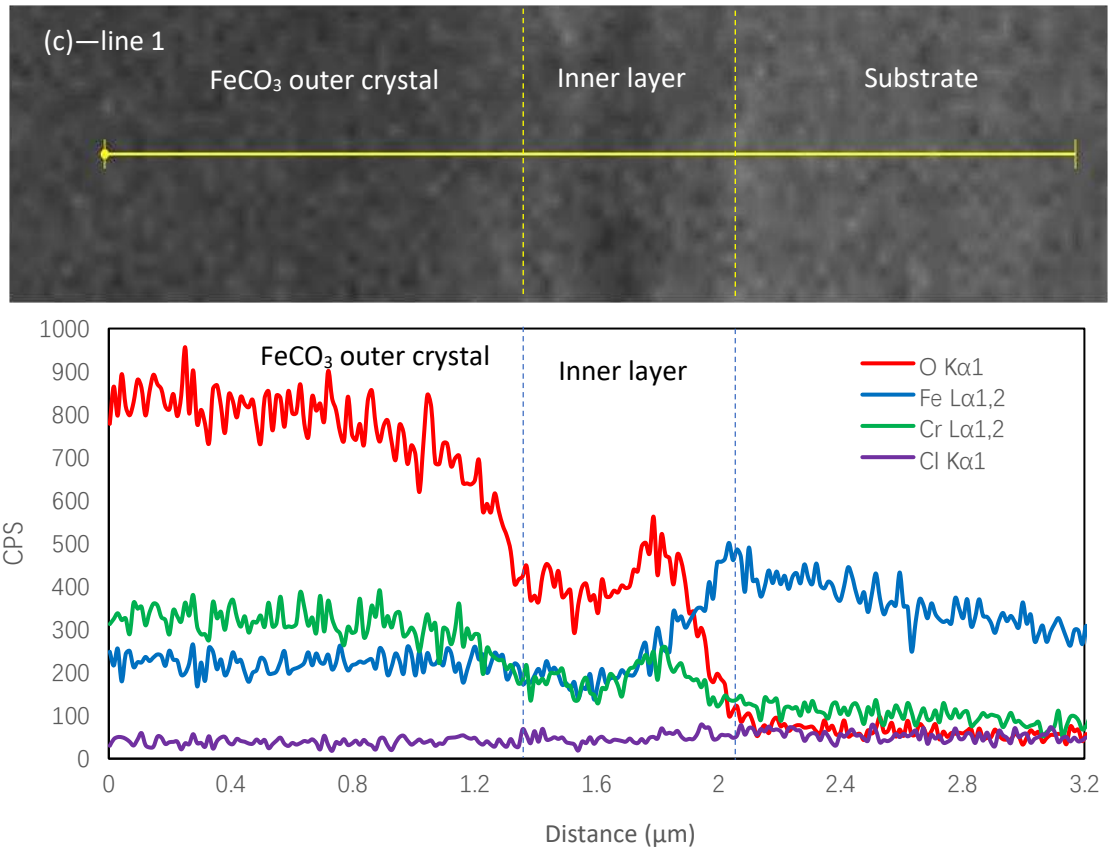

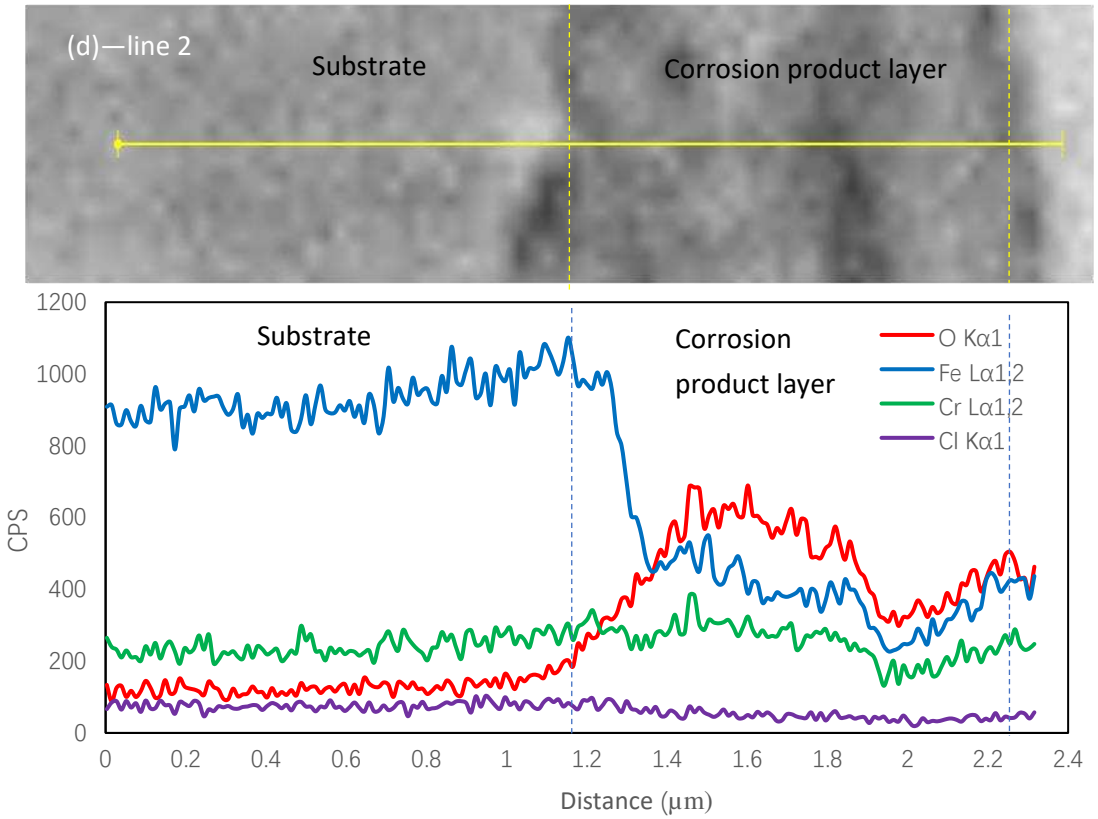

Figure 12. SEM images of analysis region (200°C and 2.7 bar p_{CO2} sample) after 20 hours, showing (a) where ion milling was performed, (b) the cross-section milled away within the surface, and EDS line-scans from (c) line-1 and (d) line-2.

Figure 13 provides the analysis region of the corrosion scales for the samples immersed in the solution at 28.5 bar of p_{CO2} and the sample was prepared via FIB. Figure 13b shows that the inner layer appears to be non-uniform, approximately between 1 and 5 μm. The localised/pitting was observed at the matrix/inner layer interface. The line-scan as shown in Figure 13c indicates that a high Cl^- concentration is contained within the inner layer, suggesting that the defects of the inner layer cause the Cl^- ions easily to penetrate, resulting in high localized corrosion occurred on the surface.

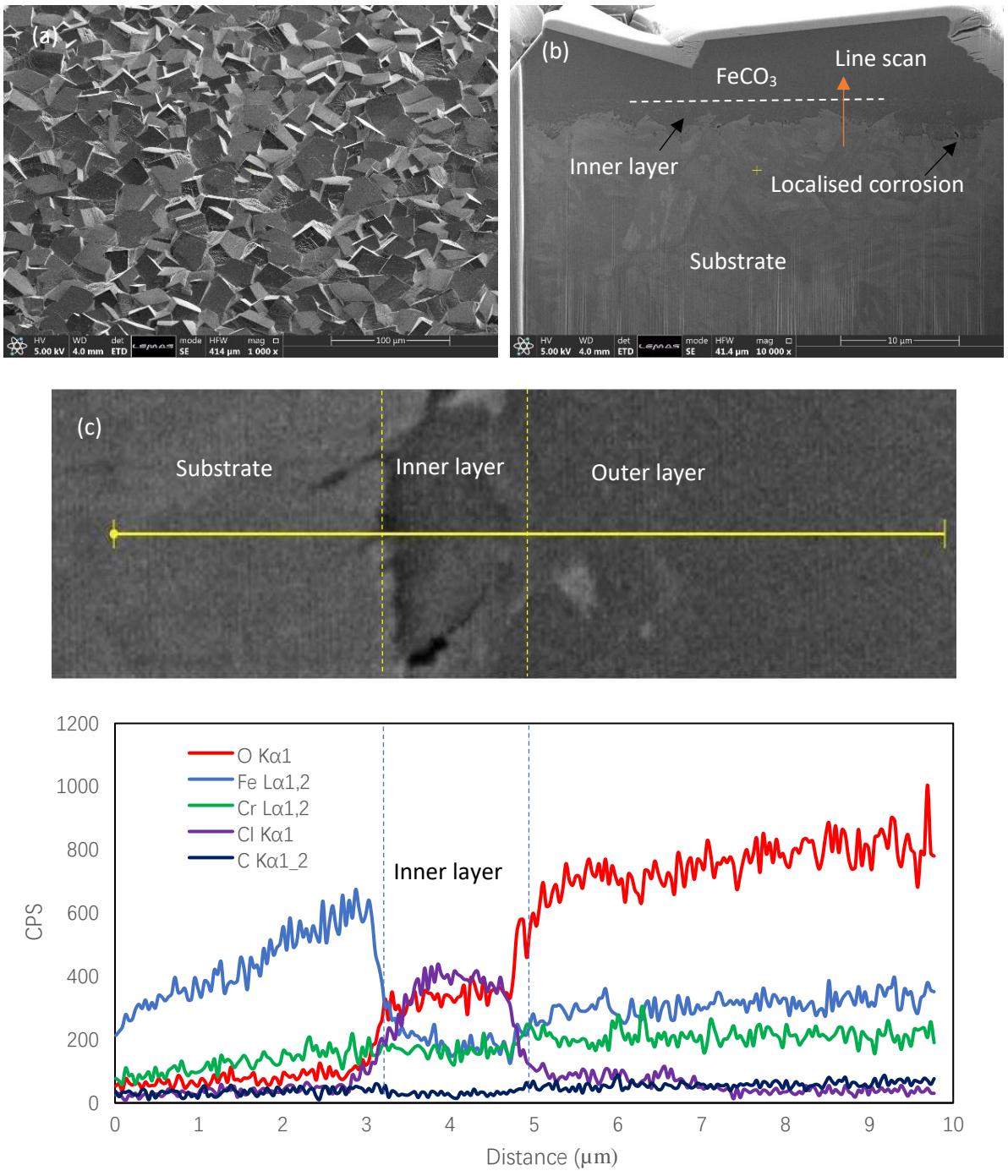

Figure 13. SEM images of analysis region (200°C and 28.5 bar p_{CO2} sample) after 20 hours, showing (a) where ion milling was performed, (b) the cross-section milled away within the surface, and (c) EDS line-scan.

4.0 Discussion

4.1 The compositions of double-layered corrosion scales for 3Cr at 2.7 bar of p_{CO2}

4.1.1 The development of the double-layered corrosion scales for Fe-H_2O-CO_2-Cl^- system at 200°C and 2.7 bar p_{CO2}

To reveal the formation of the double-layered corrosion scales on the 3Cr surface exposed to the CO_2-saturated solution at various p_{CO2} values for a constant temperature of 200°C, Pourbaix diagrams were employed to ascertain the various thermodynamically stable corrosion scales formed on the surface. Considering the relative low Cr concentration within the system since Fe is the major contributed dissolution ion in the early stage, Figure 14 illustrates the constructing Pourbaix diagram for 2.7 bar p_{CO2} conditions at 200°C for the Fe-H_2O-CO_2-Cl^- systems, where the red and purple represent solid and aqueous phases, respectively. The detected corrosion scales by XRD and Raman spectra confirmed that the corrosion scales are mainly comprised of a Fe_3O_4 inner layer and the outer $FeCO_3$ layer at 2.7 bar of p_{CO2} and 200°C after 5 hours of exposure, which is consistent with the constructing Pourbaix diagram. The potential anodic processes for the dissolution and the solid-phase formation at the surface of 3Cr steel [30, 31]:

$$Fe \leftrightarrow Fe^{2+} + 2e^- \quad (2)$$

$$3Fe^{2+} + 4H_2O \leftrightarrow Fe_3O_4(s) + 8H^+(aq) + 2e^- \quad (3)$$

$$Fe(s) + H_2CO_3(aq) + \leftrightarrow FeCO_3(s) + 2H^+(aq) + 2e^- \quad (4)$$

$$3FeCO_3(s) + 4H_2O \leftrightarrow Fe_3O_4(s) + 3H_2CO_3(aq) + 2H^+(aq) + 2e^- \quad (5)$$

The thermodynamic equilibrium electrode potential for the above reactions is presented as follows and marked as boundary lines in Figure 14.

$$E_{Fe^{2+}/Fe} = E^0_{Fe^{2+}/Fe} + \frac{2.3RT}{nF} lgc_{Fe^{2+}} \cdots\cdots\cdots line ① \quad (6)$$

$$E_{Fe_3O_4/Fe^{2+}} = E^0_{Fe_3O_4/Fe^{2+}} + \frac{2.3RT}{nF} lg\frac{c^8_{H^+}}{c^3_{Fe^{2+}}} \cdots\cdots\cdots line ② \quad (7)$$

$$E_{Fe/FeCO_3}(pH < 7.17) = E^0_{Fe/FeCO_3} + \frac{2.3RT}{2F} lg\frac{c^2_{H^+}}{c_{H_2CO_3}} \cdots\cdots\cdots line ③ \quad (8)$$

$$E_{FeCO_3/Fe_3O_4} = E^0_{FeCO_3/Fe_3O_4} + \frac{2.3RT}{2F} lgc^2_{H^+} \cdot c^3_{H_2CO_3} \cdots\cdots\cdots line ④ \quad (9)$$

In the early stage, ferrite ions are preferentially dissolved via reaction (2) and this suggests the development of Fe_3O_4 via crossing boundary ①-② at the pH below 6.38. The inner layer continuously forms and simultaneously dissolves by the equilibrium reaction (3). The ferrous ions stay thermodynamically stable in the aqueous phase (pH<6.94), indicating the consumption of the inner layer and a relatively high corrosion rate at this stage.

The development of the corrosion scales at the solution/inner layer interface leads the cathodic reactions consuming acidity via as follows:

$$2H^+(aq) + 2e^- \leftrightarrow H_2(\mathrm{g}) \quad (10)$$

$$2H_2CO_3(aq) + 2e^- \leftrightarrow 2HCO_3^-(aq) + H_2(\mathrm{g}) \quad (11)$$

$$2HCO_3^-(aq) + 2e^- \leftrightarrow 2CO_3^{2-}(aq) + H_2(\mathrm{g}) \quad (12)$$

$$2H_2O + 2e^- \leftrightarrow 2OH^-(aq) + H_2(\mathrm{g}) \quad (13)$$

347 The increase in solution pH, shifting the thermodynamic region to the $FeCO_3$ region in the
348 aqueous phase. At this stage, $FeCO_3$ replaces ferrous ions and coexists with Fe_3O_4. For the
349 prolonged time, the observation of the outer $FeCO_3$ crystals over 5 hours at 2.7 bar p_{CO2}
350 (Figure 4) verify the precipitation of $FeCO_3$ which nucleates after the supersaturation (*SR*)
351 exceeding a critical value ($SR_{critical}$):

$$SR = \frac{[\mathrm{Fe}^{2+}][\mathrm{CO}_3^{2-}]}{K_{\mathrm{SP}}} \geq SR_{\mathrm{critical}} \quad (14)$$

352 Where $[\mathrm{Fe}^{2+}]$ is the concentration of Fe^{2+}, $[\mathrm{CO}_3^{2-}]$ is the concentration of CO_3^{2-}, and K_{SP} is
353 the solubility product for $FeCO_3$[27].

354 The scattered $FeCO_3$ increases in number between 5 hours and 48 hours which corresponds
355 to a relatively high *SR*; it increases in size over 120 hours, corresponding to the decrease of
356 *SR*. The declination of *SR* indicates the improvement of the corrosion product layer against
357 Fe^{2+} diffusion, suggesting the inner layer that coexists with $FeCO_3$ is protective of the steel
358 surface, consistent with the results proposed by Hua et al. [17]. However, the development of
359 $FeCO_3$ processes is via kinetics, Pourbaix diagram is considered the thermodynamic which is
360 the limitation for this system.

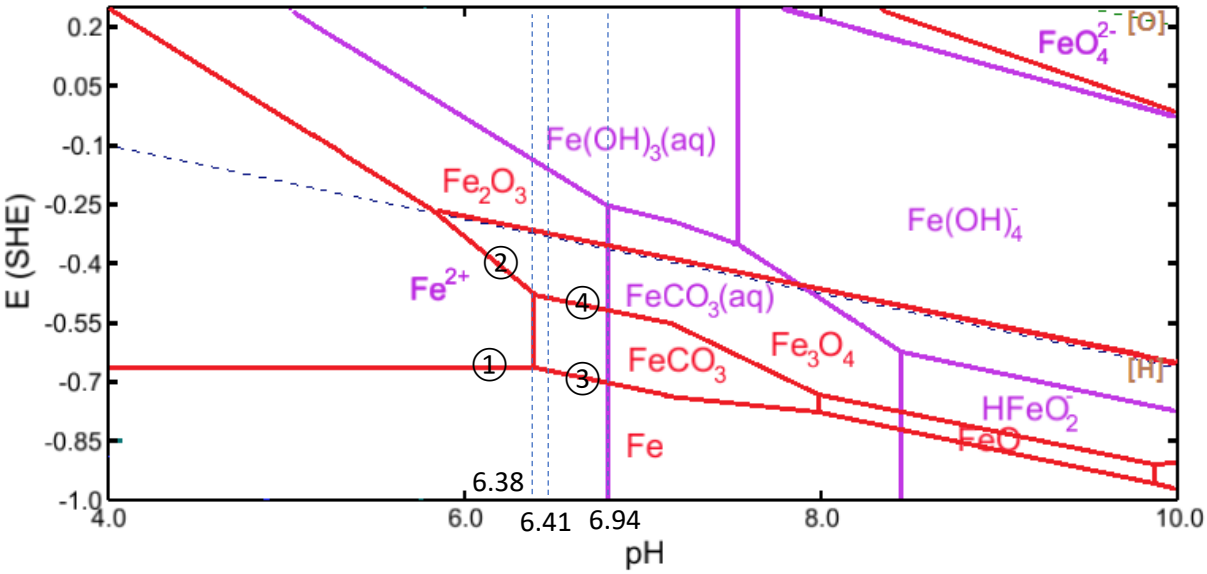

Figure 14. Pourbaix diagrams for Fe-H_2O-CO_2-Cl^- systems in the CO_2-saturated solution at 200°C and 2.7 bar p_{CO2}.

4.1.2 The development of the inner corrosion scales for the Fe-Cr-H_2O-CO_2-Cl^- systems at 200°C and p_{CO2} of 2.7 bar

The dissolution processes affect the thermodynamically stable product form on the 3Cr steel surface. [Fe^{2+}] and [Cr^{3+}] concentrations were introduced based on the mass loss of 3Cr immersed in the solution after 20 hours of exposure and simplified allocated as the elemental composition (Fe: Cr = 97 wt%: 3 wt %) for Pourbaix diagram calculation. Figure 15 illustrates the constructing Porbaix diagram for the Fe-Cr-H_2O-CO_2-Cl^- systems in comparison to the Fe-H_2O-CO_2-Cl^- systems (the calculated pH is 6.41 and corrosion potential is -0.48 V/SHE in the system) as shown in Figure 14. The Cr is considered under this circumstance due to the accumulation of Cr compounds ($FeCr_2O_4$ and $Cr(OH)_3$) during the whole corrosion processes. The formation of the spinel structure $FeCr_2O_4$ is via the reaction (15).

$$Fe(s) + 2\mathrm{Cr}^{3+} + 4H_2O \leftrightarrow FeCr_2O_4(s) + 8H^+(aq) + 2e^- \quad (15)$$

The Fe^{3+} sites occupy by Cr^{3+} in the spinel structure improves the film protectiveness of the inner layer owing to the stronger binding energy replaced by Cr-O bond[22]. The involvement of Cr in the inner layer decreases the corrosion rate as shown in Figure 3 and gradually reduces the metal ion diffusion throughout the inner layer.

Meanwhile, the accumulation of Cr^{3+} accelerates the precipitation of $Cr(OH)_3$ within the inner layer via reaction (16), which is reported as a typical compound for the Cr-bearing steels at relatively low pH environments[8, 23].

$$Cr^{3+}(aq) + 3H_2O \leftrightarrow Cr(OH)_3(aq) + 3H^+ \quad (16)$$

The precipitation of $Cr(OH)_3$ consumes alkalinity and results in a decrease of localised pH, following by subsequently enhances matrix dissolution and accelerates the formation of $FeCr_2O_4$ and $Cr(OH)_3$.

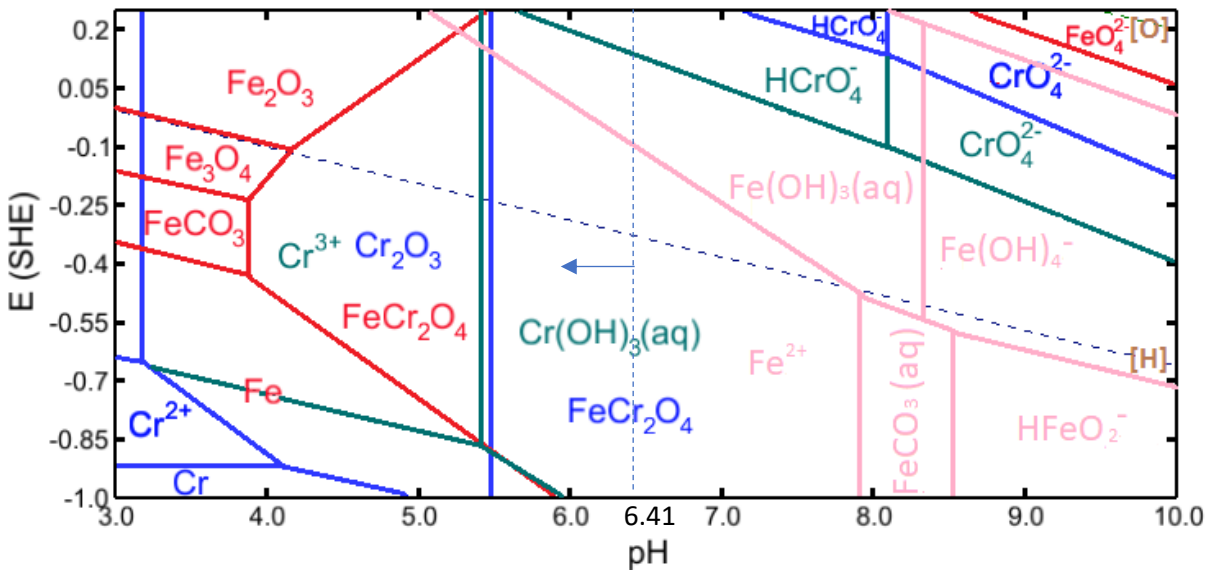

Figure 15. Pourbaix diagrams for Fe-Cr-H_2O-CO_2-Cl^- systems in the CO_2-saturated solution at 200°C and 2.7 bar p_{CO2}.

4.2 The compositions of double-layered corrosion scales for 3Cr at 28.5 bar of CO_2 partial pressure

4.2.1 The development of the double-layered corrosion scales for Fe -H_2O-CO_2-Cl^- systems at p_{CO2} of 28.5 bar

Figure 16 indicates the constructing Pourbaix diagram at 28.5 bar p_{CO2} and 200°C for Fe-H_2O-CO_2-Cl^- systems. As increasing the p_{CO2} to 28.5 bar, $FeCO_3$ becomes the thermodynamically favorable corrosion product, which presents as the extension of the thermodynamically stable region to the lower pH and noble potential in Figure 16.

Despite the enlarged $FeCO_3$ region, no thermodynamically stable solid phase can be formed in the initial stages of a system dominating by the hydrogen evolution reaction at a low pH of 5.39. The accumulation of Fe^{2+} and Cr^{3+} ions and consuming the acidity are via the cathodic reactions. The precipitation of $FeCO_3$ is via the following reaction as well as the surface pH increased at least to 5.91 and marked as boundary ⑤ as shown in Figure 16. Again, the Pourbaix diagram only considers the thermodynamic reactions, the precipitation of $FeCO_3$ over time can be controlled by the crystal kinetics.

$$Fe^{2+}(aq) + H_2CO_3(aq) \leftrightarrow FeCO_3(s) + 2H^+(aq) \quad (17)$$

$$pH_{Fe^{2+}/FeCO_3} = -\log\left(K_{(Fe^{2+}/FeCO_{3)}} \cdot c_{Fe^{2+}} \cdot c_{H_2CO_3}\right)^{\frac{1}{2}} \cdots\cdots line\ ⑤ \quad (18)$$

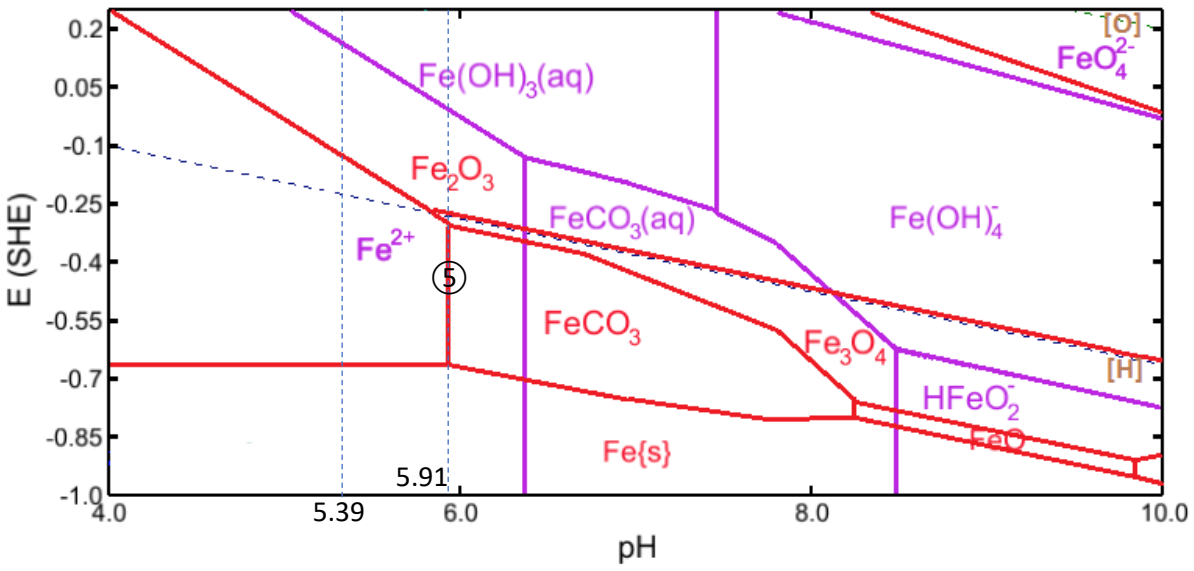

403

404 **Figure 16. Pourbaix diagrams for Fe-H_2O-CO_2-Cl^- systems in the CO_2-saturated solution at**

405 **200°C and 28.5 bar p_{CO2}.**

406 ***4.2.2 The development of the inner corrosion scales for the Fe-Cr-H_2O-CO_2-Cl^- systems at***

407 ***200°C and p_{CO2} of 28.5 bar***

408 The presence of Fe^{2+} and Cr^{3+} ions affects the thermodynamically stable product formed on

409 the 3Cr steel surface. Figure 17 illustrates the constructing Porbaix diagram for the Fe-Cr-H_2O-

410 CO_2-Cl^- systems based on the mass loss results after 20 hours in comparison to the Fe-H_2O-

411 CO_2-Cl^- systems at 28.5 bar of p_{CO2} (Figure 16). Refer to the calculate pH of 5.39 and corrosion

412 potential of -0.57 V/SHE in the system, the corrosion scales of $FeCr_2O_4$ and $Cr(OH)_3$ become

413 thermodynamically stable, and this consistent with the XRD and Raman measurements for

414 the inner layer compositions. The growth of the inner layer directly depresses the general

415 corrosion rates, and reactions (15) and (16) cause the local acidification at the matrix/inner

416 layer interface, resulting in the inner corrosion layer develops non-uniformly over long-term

417 immersion time of 120 hours as shown in 7b.

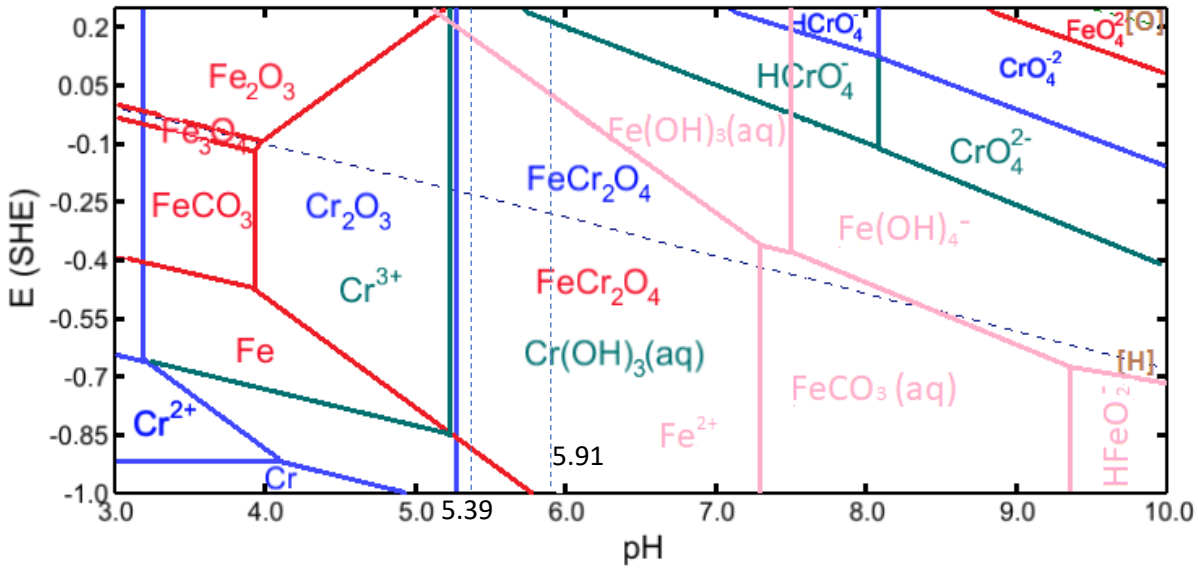

Figure 17. Pourbaix diagrams for Fe-Cr-H_2O-CO_2-Cl^- systems in the CO_2-saturated solution at 200°C and 28.5 bar p_{CO2}.

4.3 Localised corrosion of 3Cr steels induced by the formation of the inner layer containing Cl^- ions

3Cr suffered severe anodic dissolution in the initial stages at a high temperature of 200°C, which is believed to be promoted by the presence of Cl^- [25, 26]. The Cl^- ions are preferentially adsorbed on the bare surface：

$$Fe(s) + Cl^-(aq) \leftrightarrow [FeCl]^-(ads) \quad (19)$$

The formation of $[FeCl]^-$ is believed to act as a catalyse, promoting the anode dissolution process by the following mechanism [28, 29]:

$$[FeCl]^-(aq) + H_2O(l) \leftrightarrow [Fe(Cl)OH]^-(ads) + H^+(aq) + e^- \quad (20)$$

$$[Fe(Cl)OH]^-(ads) \leftrightarrow [Fe(Cl)OH](ads) + e^- \quad (21)$$

$$[Fe(Cl)OH](ads) + H^+(aq) \leftrightarrow Fe^{2+}(aq) + Cl^-(aq) + H_2O(l) \quad (22)$$

For 2.7 bar of p_{CO2}, the inner corrosion layer is rapidly covered the entire surface including the areas beneath the outer crystalline $FeCO_3$ with low recorded corrosion rates as shown in Figure 3, the Cl^- ions are blocked by the dense and compact inner layer which restrict the catalytic dissolution process, the inner layer provides good corrosion protection to the steel surface. The line-scans in Figure 12 c and d show no obvious Cl^- ions are distributed within the inner layer. A relatively mild localised corrosion for 3Cr steel without the acceleration by Cl^-, consistent with the observation of the localised corrosion shown in Figure 11.

However, according to the SEM images of the condition of 28.5 bar $p_{CO2,}$ as shown in Figure 4, the precipitation of the Cl-rich inner layer was due to the fast anodic dissolution in the initial stage, in which the positive metal irons generated and adsorbed the negative Cl^- ions, forming a Cl-rich inner layer with a defective amorphous feature. The abundance of H^+ becomes to be involved in the formation of the defects of the inner $Cr(OH)_3$ layer (Reaction 16), forming a local positive charge region and further attracting the penetration of Cl^- ions inward. The Cl^- ions accumulate at the sites where the localised acidification occurs and induce the local anodic dissolution with concentrated Cl^- ions, resulting in the sediment of the unescapable Cl^- ions within the inner layer and accelerates the localised attack. Hua et al.,[11] reported that enrichment of Cr within the product layers formed on low Cr-containing steel exhibiting to have implications for the localised corrosion. The precipitation of amorphous $Cr(OH)_3$ in the inner layer at 28.5 bar p_{CO2} and 200°C is accompanied with the severe mass loss catalysed by aggressive ions attack, such as Cl^-, provides a susceptibility for the penetration of Cl^-, resulting in the generation of the localised corrosion as shown in Figure 10.

4.4 Proposed evolution mechanism of the corrosion scales on the surface

Figure 18 indicates the schematic diagram of the formation and evolution of the corrosion scales on the 3Cr steel surface at 200°C and different p_{CO2}. The double-layered corrosion scales at low p_{CO2} of 2.7 bar mainly composes Fe_3O_4 and scattered $FeCO_3$ crystals in the early period. The covered inner layer on the substrate plays a major role in the protection of the surface compared to the outer crystalline $FeCO_3$ layer. The enrichment of Cr improved the protectiveness of the inner layer via the formation of the $FeCr_2O_4$ and $Cr(OH)_3$ but the increase in localised corrosion where the local acidification occurs during the inward growth by local anodic reactions. No obvious Cl^- accumulation exists in the corrosion scales, corresponding to a relatively low localised corrosion attack for the 3Cr samples immersed in the solution at 2.7 bar of p_{CO2} and 200°C.

For 28.5 bar p_{CO2}, the inner layer mainly composed a mixture of $FeCr_2O_4$ and $Cr(OH)_3$; and the outer layer is a compact and dense $FeCO_3$ layer. The formation of dominate $Cr(OH)_3$ at relatively low pH suggests the amorphous and highly defective features for the inner layer. The Cl^- ions easily diffuse into the defects of the inner layer, accelerating the localised corrosion at the interface where the local dissolution is catalysed by Cl^-. The formation of the Cr-riched inner layer and outer crystalline $FeCO_3$ layer enhances the protectiveness for the general corrosion. However, the results suggest that the corrosion scales are disability against the localised attacks in a Cl^--containing environment at 200°C and 28.5 bar p_{CO2}.

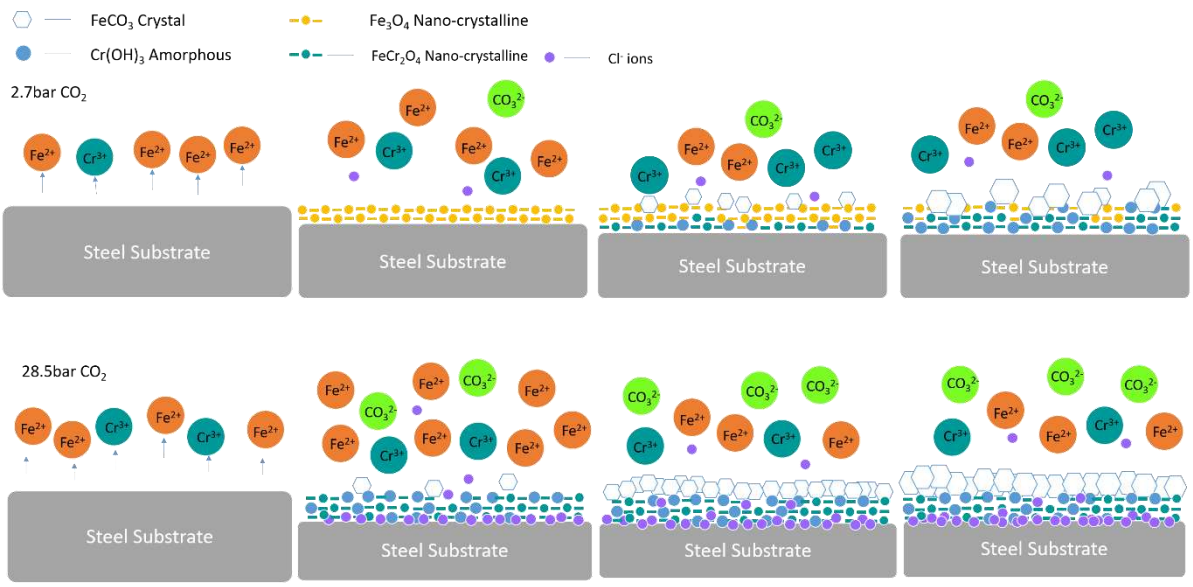

Figure 18. Schematic diagrams of the evolution of corrosion scales for 3Cr steels at 200°C and different p_{CO2}.

5.0 Conclusions

The characterisation of the double-layered corrosion scales on the surface and the localised corrosion behaviour of 3Cr steel under a geothermal environment has been investigated at 2.7 and 28.5 bar of p_{CO2} for a constant temperature of 200°C. The study is mainly focused on the corrosion behaviour and the evolution of the corrosion product scales on the 3Cr surface. The following main conclusions can be made:

1. At 200°C and 2.7 bar of p_{CO2}, the developed corrosion product scales on 3Cr include three periods: for period I, the formation of inner Fe_3O_4-dominated layer (containing small amount of $Cr(OH)_3$) and the precipitation of outer $FeCO_3$ crystals; Stage II, Fe_3O_4 transited to $FeCr_2O_4$ and $Cr(OH)_3$ precipitation. Stage III, the growth of the crystalline $FeCO_3$.

2. The outer layer of corrosion product scales for 3Cr steel at 200°C and 2.7 bar of p_{CO2} are

scattered crystalline $FeCO_3$ outer layer and an inner layer composes of $FeCr_2O_4$ and $Cr(OH)_3$ over 120 hours of exposure.

3. For the condition of 28.5 bar of p_{CO2}, the corrosion scales are mainly comprised of the outer crystalline $FeCO_3$ and inner layers of $FeCr_2O_4$ and $Cr(OH)_3$. The formation of the crystalline $FeCO_3$ layer is dense and compact after 5 hours in comparison to the scattered $FeCO_3$ crystals observed at 2.7 bar of p_{CO2}.

4. The formation of the corrosion layers at 28.5 bar of p_{CO2} acts as a barrier against general corrosion. However, the localised corrosion is high due to the level of Cl^- content within the inner layer at 28.5 bar of p_{CO2}, which accelerates the localised attacks compared to 2.7 bar after 120 hours of immersion.

Acknowledgements

This work is supported by the Postdoctor Research Foundation of Shunde Graduate School of University of Science and Technology Beijing (No. 2020BH013). We would like to thank Mr. John Harrington, Dr Zabeada Aslam and Mr. Stuart Micklethwaite from the University of Leeds, Electron Microscopy and Spectroscopy Centre (LEMAS) for the assistance with FIB measurements.

6.0 Reference

1. L. Xu, S. Guo, C. Gao, W. Chang, T. Chen, and M. Lu, Influence of microstructure on mechanical properties and corrosion behavior of 3% Cr steel in CO_2 environment. Materials and Corrosion, 2012. 63(11): p. 997-1003.
2. T. Muraki, T. Hara, and H. Asahi. Effects of chromium content up to 5% and dissolved oxygen on CO_2 corrosion. in CORROSION 2002. 2002. NACE International.
3. M. Ueda. and H. Takabe. The formation behavior of corrosion protective films of low Cr bearing steels in CO_2 environments. in CORROSION 2001. 2001. NACE International.
4. B. Kermani, J.C. Gonzales, G.L. Turconi, L. Pigliacampo, T. Perez, and C. Morales. Window of application and operational track record of low carbon 3Cr steel tubular. in CORROSION 2006. 2006. NACE International.
5. J. Zhu, L. Xu, and M. Lu, Electrochemical impedance spectroscopy study of the corrosion of 3Cr pipeline steel in simulated CO_2-saturated oilfield formation waters. Corrosion, 2015. 71(7): p. 854-864.
6. S. Guo, L. Xu, L. Zhang, W. Chang, and M. Lu, Characterization of corrosion scale formed on 3Cr steel in CO_2-saturated formation water. Corrosion Science, 2016. 110: p. 123-133.
7. Y. Lu, H. Jing, Y. Han, and L. Xu, Effect of temperature on the 3Cr low-alloyed steel initial corrosion behavior in CO_2 solution. Materials Chemistry and Physics, 2016. 178: p. 160-172.
8. H.F. Liu, D. Han, J. Sun, and Y. Hua. Applicability of 3Cr-N80 Steel and N80 Steel in Oilfield CO_2 Environment. in CORROSION 2019. 2019. NACE International.

9. W. Li, L. Xu, L. Qiao, and J. Li, Effect of free Cr content on corrosion behavior of 3Cr steels in a CO_2 environment. Applied Surface Science, 2017. 425: p. 32-45.
10. B. Wang, L. Xu, G. Liu, and M. Lu, Corrosion behavior and mechanism of 3Cr steel in CO_2 environment with various Ca^{2+} concentration. Corrosion Science, 2018. 136: p. 210-220.
11. Y. Hua, S. Mohammed, R. Barker, and A. Neville, Comparisons of corrosion behaviour for X65 and low Cr steels in high pressure CO_2-saturated brine. Journal of Materials Science & Technology, 2020. 41: p. 21-32.
12. C. Chen, M. Lu, D. Sun, Z. Zhang, and W. Chang, Effect of chromium on the pitting resistance of oil tube steel in a carbon dioxide corrosion system. Corrosion, 2005. 61(6): p. 594-601.
13. X. Lin, W. Liu, F. Wu, C. Xu, J. Dou, and M. Lu, Effect of O_2 on corrosion of 3Cr steel in high temperature and high pressure CO_2–O_2 environment. Applied Surface Science, 2015. 329: p. 104-115.
14. L. Wei, and K. Gao, Understanding the general and localized corrosion mechanisms of Cr-containing steels in supercritical CO_2-saturated aqueous environments. Journal of Alloys and Compounds, 2019. 792: p. 328-340.
15. ASTM, E3-01. 2002: Standard Practice for Preparation of Metallographic Specimens. Annual Book of ASTM Standards, ASTM.
16. ASTM, E 407–99, Standard Guide for Microetching Metals and Alloys. American Society for Testing Materials.

17. Y. Hua, S. Xu, Y. Wang, W. Taleb, J. Sun, L. Zhang, R. Barker, and A. Neville, The formation of $FeCO_3$ and Fe_3O_4 on carbon steel and their protective capabilities against CO_2 corrosion at elevated temperature and pressure. Corrosion Science, 2019. 157: p. 392-405.

18. Y. Hua, R. Barker, and A. Neville, Effect of temperautre on the critical water content for general and localised corrosion of X65 carbon steel in the transport of supercritical CO_2. The International Journal of Greenhouse Gas Control, 2014. 31: p. 48-60.

19. ASTM, Standard G1-03, Standard practice for preparing, cleaning, and evaluating corrosion test specimens. ASTM International: West Conshohocken, PA, 2003.

20. ASTM, Standard G46-94, Standard guide for examination and evaluation of pitting corrosion. ASTM International: West Conshohocken, PA, 2003.

21. X. Yue, L. Zhang, Y. Wang, S. Xu, C. Wang, M. Lu, A. Neville, and Y. Hua, Evolution and characterization of the film formed on super 13Cr stainless steel in CO_2-saturated formation water at high temperature. Corrosion Science, 2019: p. 108277.

22. Y. Li, T. Xu, S. Wang, B. Fekete, J. Yang, J. Yang, J. Qiu, A. Xu, J. Wang, and Y. Xu, Modelling and analysis of the corrosion characteristics of ferritic-martensitic steels in supercritical water. Materials, 2019. 12(3): p. 409.

23. L. Xu, S. Guo, W. Chang, T. Chen, L. Hu, and M. Lu, Corrosion of Cr bearing low alloy pipeline steel in CO_2 environment at static and flowing conditions. Applied surface science, 2013. 270: p. 395-404.

24. OLI software V -2.2 (OLI engine + CPS module), OLI System Ins., Morris Plains, NJ, 2016.

564 25. D.D. Macdonald, Passivity–the key to our metals-based civilization, Pure and Applied
565 Chemistry. 71 (1999) 951–978.
566 26. Y. Zhao, X. Li, C. Zhang, T. Zhang, J. Xie, G. Zeng, D. Xu, F. Wang, Investigation of the
567 rotation speed on corrosion behavior of HP-13Cr stainless steel in the extremely
568 aggressive oilfield environment by using the rotating cage test, Corrosion Science. 145
569 (2018) 307–319.
570 27. S. Nesic, N. Thevenot, J.L. Crolet, D. Drazic, Electrochemical Properties of Iron
571 Dissolution in the Presence of CO_2 - Basics Revisited, in: NACE-96003, NACE
572 International, Denver, Colorado, 1996: p. 23.
573 28. M.A.J. Mazumder, H.A. Al-Muallem, M. Faiz, S.A. Ali, Design and synthesis of a novel
574 class of inhibitors for mild steel corrosion in acidic and carbon dioxide-saturated saline
575 media, Corrosion Science. 87 (2014) 187–198.
576 29. T.Tanupabrungsun, D. Young, B. Brown, S. Nesic, Construction and verification of
577 Pourbaix diagrams for CO_2 corrosion of mild steel valid up to 250 °C, in: NACE-2012-
578 1418. NACE International, NACE, 2012:p.16.
579 30. Q. Yang , L. J. Qiao, S. Chiovelli, J. L. Luo. Effects of hydrogen on pitting susceptibility of
580 type 310 stainless steel. Corrosion, 1998, 54(8): p. 628-633.
581 31. J. B. Sun, W. Liu, W. Chang, Z. H. Zhang, Z. T. Li, T. Yu and M. X. Lu. Characterisation and
582 formation mechanism of corrosion scales on low-chromium X65 steels in CO_2
583 environment. Acta Metall Sin 45.1 (2009): 84-90.